

**Proper Plasma Analysis Practice (PPAP),
an Integrated Procedure of the Extinction Correction and Plasma Diagnostics:
a Demo with an HST/WFC3 Image Set of NGC 6720**

TOSHIYA UETA (植田稔也)^{1,2,3} AND MASAOKI OTSUKA (大塚雅昭)²

¹*Department of Physics and Astronomy, University of Denver, 2112 E. Wesley Ave., Denver, CO 80208, USA*

²*Okayama Observatory, Kyoto University, Honjo, Kamogata, Asakuchi, Okayama, 719-0232, Japan*

³*JSPS Invitation Fellow for Research in Japan (FY2020, long-term)*

(Received June 27, 2021; Revised August 2, 2021; Accepted August 24, 2021)

Submitted to PASP Tutorial

ABSTRACT

In this work, we propose a proper plasma analysis practice (PPAP), an updated procedure of plasma diagnostics in the era of spatially-resolved spectroscopy. In particular, we emphasize the importance of performing both of the extinction correction and the direct method of plasma diagnostics simultaneously as an integrated process. This approach is motivated by the reciprocal dependence between critical parameters in these analyses, which can be resolved by iteratively seeking a converged solution. The use of PPAP allows us to eliminate unnecessary assumptions that prevent us from obtaining an exact solution at each element of the spectral imaging data. Using a suite of *HST*/WFC3 narrow-band images of the planetary nebula, NGC 6720, we validate PPAP by (1) simultaneously and self-consistently deriving the extinction, $c(\text{H}\beta)$, and electron density/temperature distribution, ($n_e([\text{S II}])$, $T_e([\text{N II}])$), maps that are consistent with each other, and (2) obtaining identical metal abundance distribution maps, ($n(\text{N}^+)/n(\text{H}^+)$, $n(\text{S}^+)/n(\text{H}^+)$), from multiple emission line maps at different wavelengths/transition energies. We also determine that the derived $c(\text{H}\beta)$ consists both of the ISM and circumsource components and that the ionized gas-to-dust mass ratio in the main ring is at least 437 and as high as about 1600. We find that, unless we deliberately seek self-consistency, uncertainties at tens of % can easily arise in outcomes, making it impossible to discern actual spatial variations that occurs at the same level, defeating the purpose of conducting spatially resolved spectroscopic observations.

Keywords: Astronomy data reduction (1861) — Direct imaging (387) — Spectroscopy (1558) — Photoionization (2060) — Extinction (505) — H II regions (694) — Planetary nebulae (1249)

1. INTRODUCTION

Plasma diagnostics are fundamental to understanding the physical conditions of various gaseous systems (e.g. Osterbrock & Ferland 2006; Kewley et al. 2019). The relative strengths of various diagnostic emission lines determine the excitation states of specific gaseous species, yielding their electron densities and temperatures, and subsequently, metal abundances (e.g. Peimbert et al. 2017; Nicholls et al. 2020). However, these emission lines required in plasma diagnostics must first be corrected for both the interstellar and circumsource extinction by adopting a suitable extinction law, especially when the amount of extinction is not really negligible (e.g. Draine 2003; Salim & Narayanan 2020). This is the quintessence of observational astronomy, in which

all measurements made from a distance are affected by extinction.

The determination of extinction is far from a trivial task. Practically, the amount of extinction is usually determined, for example, by comparing the observed diagnostic H I recombination line ratio with its theoretical expectation (i.e. the intrinsic line ratio without extinction). The theoretical line ratios can be computed for specific electron density (n_e) and temperature (T_e) of the target emitting gas (e.g. Hummer & Storey 1987; Storey & Hummer 1995). Obviously, n_e and T_e are the very quantities to be figured out by plasma diagnostics using *extinction-corrected* line ratios. Hence, this is a classic catch-22 situation. Therefore, to overcome this conundrum, plasma diagnostics ought to be performed

together with the extinction determination/correction as a single integrated process.

However, what is traditionally exercised in the literature has been to introduce a number of simplifications. For example, *ad hoc* n_e and T_e may be chosen to force a value of extinction to get the subsequent plasma diagnostics going, or an *ad hoc* extinction value may even be adopted. In such cases, one should at least guarantee consistency between the *assumed* n_e and T_e values as the bases for the *assumed* extinction and the n_e and T_e values as the actual outcomes of the subsequent plasma diagnostics. In other words, the initially assumed n_e and T_e values cannot be very different from the final n_e and T_e values to assure that these n_e and T_e values represent the ionized gas in the target object. In practice, the subtlety of such consistency tends to be lost in translation, because the extinction determination and plasma diagnostics are often dealt with as two separate issues. Hence, consistency between these two sets of n_e and T_e is rarely scrutinized, let alone guaranteed. Consequently, such inconsistencies would usually invite uncertainties, albeit inadvertently.

Meanwhile, spatially resolved 2-D plasma diagnostics have been becoming very relevant lately in many branches of astronomy and astrophysics, especially with the increasing availability of integral field spectrographs (e.g. Walsh & Monreal-Ibero 2020). When measurements of extended target sources are made in a spatially resolved manner, both the extinction determination and plasma diagnostics ought to be performed at each detector element. It is to ensure that the spatially extended nature of the target sources is fully appreciated at the end of the analyses.

However, the spatial variation of relevant parameters in extended objects has rarely been considered carefully enough in both the extinction determination and plasma diagnostics. Often a single-valued extinction is adopted by assuming uniform n_e and T_e across the whole extent of an extended object (e.g. Lamé & Pogge 1994; Guerrero et al. 1997). Such simplifications may be permissible as long as the aim is to sample representative quantities of an extended object in an integrated sense. Regrettably, such a deed defeats the purpose of spatially resolved observations, by forcing an extended object with artificial uniformity, i.e., imposing an absolutely unnecessary source of uncertainties.

In the present work, therefore, we propose a procedure that streamlines both the extinction correction and plasma diagnostics as a single integrated process of iterative data reduction. By seeking convergence at each spatial element through this iterative process, we can simultaneously and self-consistently determine the extinction map as well as the electron density/temperature (n_e and T_e) maps, which allow us to carry out a plethora of spatially-resolved analyses. Below, we demonstrate and validate the process in detail using a full suite of the archived Hubble Space Telescope (*HST*)/WFC3 nar-

rowband images of the Galactic planetary nebula (PN), NGC 6720.

First, we briefly describe the adopted data and the line calibration applied, before we detail the iterative procedure (§2). We then derive the extinction map (§3.1), n_e ([S II]) and T_e ([N II]) maps (§3.2), and extinction-corrected line emission maps (§3.4), as well as metal abundance distribution maps (§3.5), while giving detailed discussion of the outcomes and contrasting between the present results and those obtained with typical simplifications (§3.7). In the end, we summarize and promote one of the most self-consistent and fully 2-D plasma diagnostics ever performed (§4).

2. ANALYSES

2.1. WFC3 Narrowband Image Set of NGC 6720

For the present study, we adopt images of the planetary nebula, NGC 6720, stored in the Hubble Legacy Archive¹. These images were taken with the WFC3 camera on 2011 September 19 and 25 as part of the program 12309 (PI: C. R. O’Dell; O’Dell et al. 2013a,b,c). We adopt this data set because this program is one of the few that used the exquisite suite of the WFC3 narrowband filters most extensively, providing an excellent opportunity to perform self-consistent plasma diagnostics in full 2-D based on narrowband images and compare the results with those of the previous investigations.

Table 1 lists all the filters used in this program, with their average wavelength and rectangular width (according to PYSYNPHOT; Lim et al. 2015) and “official” description (Dressel 2019). However, the F953N image is not used because of the known severe fringe pattern (Wong 2010; also §5.4.4 of Dressel 2019). The “Q” in a filter name stands for a “QUAD” filter, which refers to one of the 2×2 mosaic of four filters providing four different bandpasses simultaneously with each band covering a quarter of the nominal field of view (FoV: Dressel 2019). Because of the smaller field coverage of the QUAD filters, the subsequent analyses are all restricted within the NW quadrant of the main ring structure of NGC 6720 (see below; also see the Shared Field of View of All Filters in Fig. 2 of O’Dell et al. 2013a and Figs. 4d,e of Ueta et al. 2019).

2.2. The QP Method

Many WFC3 filters can isolate the target emission line reasonably well. However, some filters suffer from unavoidable blending of neighboring lines at comparable strengths (Appendix A.2 of Dressel 2019). The most critical is the F656N and F658N filter pair. Even though the F656N and F658N filters are officially described as the H α and [N II] filters, respectively (Table 1), their transmission profiles cover both the H α and [N II] lines

¹ <https://hla.stsci.edu/>

Filter	λ (Å)	$\Delta\lambda$ (Å)	Official Description
FQ436N	4367.21	43.35	H γ 4340 Å+[O III] 4363 Å
FQ437N	4371.09	29.99	[O III] 4363 Å
F469N	4688.14	49.68	He II 4686 Å
F487N	4871.42	60.40	H β 4861 Å
F502N	5009.70	65.29	[O III] 5007 Å
F547M	5451.08	649.14	Strömgren y (continuum)
FQ575N	5757.87	18.37	[N II] 5755 Å
F645N	6453.71	84.22	continuum
F656N	6561.45	17.65	H α 6563 Å
F658N	6584.95	27.56	[N II] 6583 Å
FQ672N	6716.62	19.37	[S II] 6717 Å
F673N	6766.05	117.77	[S II] 6717/31 Å
FQ674N	6730.77	17.63	[S II] 6731 Å
FQ750N	7502.55	70.43	continuum
F953N	9530.92	97.04	[S III] 9532 Å

Table 1. *HST*/WFC3 filters used in the Program 12309. The quoted values are the bandpass average wavelength (λ) and bandpass rectangular width ($\Delta\lambda$) defined in PYSYNPHOT (Lim et al. 2015).

(Lim et al. 2015). As a result, both of the F656N and F658N images are blends of H α and [N II] lines at different proportions.

To address this line-blending issue of narrowband filter images, we developed a new calibration method based on Quadratic Programming (QP), dubbed the QP line extraction method (Ueta et al. 2019). Using the *HST* images of NGC 6720 in the F656N and F658N filters in comparison with the ground-based slit-scan spectral imaging data cube around H α , we demonstrated that the QP method properly extracted the individual H α -only and [N II]-only line maps from the line-blended raw F656N and F658N images (Ueta et al. 2019).

The QP method recognizes narrowband images that are affected by line blending as linear combinations of emission maps of blended lines, each of which is modulated by the system throughput at the wavelength of the blended lines. Provided that the underlying continuum is properly subtracted, and assuming that all the lines involved are sufficiently narrow (i.e. a line can be specified by a single wavelength), the solution for such a set of linear equations can then be sought as a QP problem in a least-squares sense under the presence of appropriate constraints. For the present work, we isolate the H α and [N II] 6548/83 Å line maps from the F656N and F658N images, the [S II] 6717/31 Å line maps from the FQ672N, F673N, and FQ674N images, and the [O III] 4363 Å and H γ maps from the FQ436N and FQ437N images. As the QP processing itself is already described

fully elsewhere (Ueta et al. 2019), we outline how these images are processed in Appendix A.

Here, we emphasize that the QP line calibration method is more advantageous than other methods that attempt to remove the fractional contribution of the unwanted blended lines by just scaling the raw images (e.g. Appendix of O’Dell et al. 2013a). Such scaling methods are strictly dependent on the line emission distribution of the raw line-blended images. That is, the line emission distribution of an isolated target line is always the same as that of the raw line-blended image that mimics the the distribution of the target line.

In reality, however, the line emission distribution of the blended lines represents neither that of the target line nor that of the blended line (as it is a mix of the two): the resulting de-blended line emission maps do not have to appear the same as the raw line-blended images. Instead, the QP method can recover the emission distribution of individual lines as the optimized solution of a QP problem on a pixel-to-pixel basis. This is what makes the QP method unique in comparison with other line calibration methods for narrowband images.

2.3. Iterative Determination of $c(\text{H}\beta)$ and (n_e, T_e)

The apparent interdependence among the extinction and (n_e, T_e) may not have been taken into consideration with a sufficient amount of attention that it deserves for some unknown reason(s). As outlined in §1, to derive the extinction and (n_e, T_e) self-consistently by breaking the circular logic behind the theories of extinction and astrophysical plasma, both the extinction determination and plasma diagnostics must be performed simultaneously as one integrated process. In the following subsections, we establish an iterative process through which this interdependence among the extinction and (n_e, T_e) is carefully addressed.

2.3.1. Extinction Correction

We start by defining $c(\lambda)$, the extinction at some wavelength, λ , as the base-10 power-law index to describe the reduction of the intrinsic flux, $I_0(\lambda)$, to the observed flux, $I(\lambda)$, by

$$I(\lambda) = I_0(\lambda) \times 10^{-c(\lambda)}. \quad (1)$$

Then, we can determine $c(\text{H}\beta)$, the extinction at H β , using, for example, the observed-to-intrinsic H α -to-H β flux ratio via

$$c(\text{H}\beta) = \frac{-\log_{10} \frac{I(\text{H}\alpha)/I(\text{H}\beta)}{I_0(\text{H}\alpha)/I_0(\text{H}\beta)}}{\frac{A_{\text{H}\alpha} - A_{\text{H}\beta}}{A_{\text{H}\beta}}}. \quad (2)$$

Here, $c(\text{H}\alpha)/c(\text{H}\beta)$ has been replaced by $A(\text{H}\alpha)/A(\text{H}\beta)$, where $A(\lambda)$ is the total extinction at λ (the extinction on the magnitude basis) and $A(\lambda) = 2.5 \times c(\lambda)$ because

$$I(\lambda) = I_0(\lambda) \times 10^{-\frac{A(\lambda)}{2.5}}. \quad (3)$$

We can thus define the observed flux at λ relative to the $H\beta$ flux as

$$\begin{aligned} \frac{I(\lambda)}{I(H\beta)} &= \frac{I_0(\lambda) \times 10^{-c(\lambda)}}{I_0(H\beta) \times 10^{-c(H\beta)}} \\ &= \frac{I_0(\lambda)}{I_0(H\beta)} 10^{-(c(\lambda)-c(H\beta))}, \end{aligned} \quad (4)$$

from which $c(\lambda)$ can be determined via

$$\begin{aligned} c(\lambda) &= -\log_{10} \left(\frac{I(\lambda)/I(H\beta)}{I_0(\lambda)/I_0(H\beta)} \right) + c(H\beta) \\ &= c(H\beta) \left(\frac{A_\lambda - A_{H\beta}}{A_{H\beta}} + 1 \right) \\ &= c(H\beta) \left(\frac{A_\lambda}{A_{H\beta}} \right) \\ &\approx c(H\beta) \cdot \left\langle \frac{A_\lambda}{A_V} \right\rangle / \left\langle \frac{A_{H\beta}}{A_V} \right\rangle, \end{aligned} \quad (5)$$

given that we know $c(H\beta)$ and the extinction curve, $\langle A_\lambda/A_V \rangle$ (the average extinction at λ relative to V), which is provided by some extinction law (e.g. [Draine 2003](#); [Salim & Narayanan 2020](#)). Then, we can recover the intrinsic line flux map at any λ from the observed line flux map at λ via Eq. (1).

An obvious caveat here is the choice of the extinction law, and the total-to-selective extinction, R_V , which scales the selected extinction curve. Thus, the value of R_V along the line of sight to the target object must be evaluated properly before we go any further. For the present study, we opt to adopt the Galactic extinction law of [Cardelli et al. \(1989, CCM, hereafter\)](#), as the present analyses are concerned with data in the optical, in which there is little difference among the existing extinction laws. As for R_V , we use the value of 3.13 ± 0.03 to the direction of NGC 6720, interpolated from R_V values determined for nearby stars within a 0.5° radius ([Gontcharov 2012](#); [Gontcharov & Mosenkov 2017](#)). We assume that R_V is uniform over NGC 6720, as the adopted data by [Gontcharov \(2012\)](#) and [Gontcharov & Mosenkov \(2017\)](#) do not have sufficient spatial resolution.

Another even more subtle but no less insignificant caveat is the choice of the theoretical $H\alpha$ -to- $H\beta$ line flux ratio, which is required to derive $c(\lambda)$ via Eqs. (2) and (5). Here, we need to remind ourselves that the theoretical $H\alpha$ -to- $H\beta$ line flux ratio is really a function of n_e and T_e of the emitting gas of the target (e.g. [Storey & Hummer 1995](#)). Hence, the determination of the interstellar extinction is actually dependent on n_e and T_e of the target object, which are the very quantities that we seek. Therefore, the present series of processes to determine $c(H\beta)$ and (n_e, T_e) must truly be performed as an integrated iterative procedure seeking the convergence of all of these values.

However, such an iteration is hardly exercised in practice: usually n_e and T_e are assumed to be some ‘‘typical’’ values. This exercise *may be* permissible as long as target sources are unresolved and the adopted n_e and T_e values are consistent with values derived as a result of the subsequent plasma diagnostics. However, when we expect these quantities to vary spatially in extended objects, we ought to perform this iterative process rigorously in each spatial element of the input images.

Therefore, for the present study, we first adopt $n_e = 10^3 \text{ cm}^{-3}$ and $T_e = 10^4 \text{ K}$ as the *initial values*. The *initial* n_e and T_e values then yield the *initial* theoretical $I_0(H\alpha)/I_0(H\beta)$ ratio of 2.858 under the Case B/optically thick condition ([Storey & Hummer 1995](#)) with the CCM extinction law and $R_V = 3.13$. Here, we stress that the theoretical $H\alpha$ line ratio needed in determining the extinction *does* depend on n_e and T_e . In the literature, this fundamental dependence is often neglected and the ratio is set to 2.85 or thereabout without any reference to the assumed n_e and T_e values, which may be different from $n_e = 10^3 \text{ cm}^{-3}$ and $T_e = 10^4 \text{ K}$. In the present work, however, these values are iteratively updated for convergence (so is the theoretical $H\alpha$ line ratio) to *ascertain the optimum consistency* between plasma diagnostics and extinction correction.

In addition, we note that extinction toward a target is not necessarily just of interstellar origin. The target object itself may be surrounded by its own obscuring agents (i.e. dust grains) contributing to the circumsource extinction, on top of what is caused by the interstellar medium (ISM). For evolved stars such as NGC 6720, the circumstellar matter (CSM) most likely causes a significant amount of the CSM extinction. Hence, if the ISM extinction is hastily adopted as the intrinsic extinction toward a target source with a substantial circumsource extinction, the corresponding $c(H\beta)$ value toward the source is bound to be underestimated.²

The mean $E(B - V)$ reddening toward NGC 6720 is reported to be 0.0870 ± 0.0005 ([Schlegel et al. 1998](#)). Under the CCM extinction law with $R_V = 3.13$, the reported $E(B - V)$ translates to $c(H\beta)$ as 0.1266 ± 0.0007 via

$$R_V = \frac{A_V}{E(B - V)} = \frac{2.5c(V)}{E(B - V)} = \frac{2.5c(H\beta)}{E(B - V)} \left\langle \frac{A_V}{A_{H\beta}} \right\rangle.$$

This means that $c(H\beta)$ to be obtained in the present analysis for NGC 6720 has to be greater than 0.1266. Any excess extinction to be detected toward NGC 6720 in the present work, therefore, is the CSM extinction component contributed by the circumstellar dust grains, which is not accounted for by any of the ISM extinction studies (e.g. [Schlegel et al. 1998](#)). This is true, of course,

² For example, using the Galactic Dust Reddening and Extinction tool made available via <https://irsa.ipac.caltech.edu/applications/DUST/>

only if the obscuring property of the circumstellar matter follows that of the adopted ISM dust grains (CCM for the present case).

2.3.2. Plasma Diagnostics

In performing plasma diagnostics, atoms are represented as n -level energy states. Then, n_e and T_e are determined by solving a set of equilibrium equations for the adopted n levels. In these equilibrium equations, the collisional excitation coefficient has $n_e T_e^{1/2} \exp(-\Delta E/kT_e)$ dependence (where ΔE is the energy difference between any two levels) and the collisional de-excitation coefficient has $n_e T_e^{1/2}$ dependence, while the radiation de-excitation coefficient has dependence on neither n_e nor T_e to the first order (Osterbrock & Ferland 2006; Pradhan & Nahar 2015).

Thus, if we take the ratio between lines whose transition energies are close to each other (i.e. $\Delta E \sim 0$; e.g. the [S II] 6731-to-6717 Å ratio), such ratios can depend *mostly* on n_e and only weakly on T_e . On the contrary, if we take the ratio between lines whose transition energies are very different (e.g. the [N II] 5755-to-6583 Å ratio), such ratios can depend *mainly* on T_e and only weakly on n_e . Then, we can find n_e and T_e as the point in the n_e - T_e space at which these two diagnostic line ratio curves intersect (see, also, §3.7.1). As this point can not be computed analytically, n_e and T_e have to be evaluated numerically by iteration.

For this work, we use the [S II] 6731-to-6717 Å line ratio map and the [N II] 5755-to-6583 Å line ratio map as the input diagnostic line ratio maps. In addition, the present set of data offers the [O III] 4363-to-5007 Å line ratio as another diagnostic for higher excitation regions than those probed via the [N II] 5755-to-6583 Å line ratio. However, the *HST*/WFC3 narrowband filter set does not offer any diagnostic ratio appropriate to prove higher excitation regions with the [O III] 4363-to-5007 Å line ratio. Hence, we will not use the [O III] 4363-to-5007 Å line ratio (but will come back to this point later in §3.7.1). This forced choice of diagnostic line ratios, however, is not necessarily bad, because the spatial extent of [S II] and [N II] is similar to that of H α and H β , covering the main ring structure of NGC 6720. For the subsequent discussion, we always refer to n_e and T_e as $n_e([\text{S II}])$ and $T_e([\text{N II}])$ with the diagnostic line used to explicitly indicate relevant energy regimes.

2.3.3. Iterative Procedure

It is not too difficult to imagine that deriving $c(\text{H}\beta)$ and (n_e, T_e) that simultaneously satisfy extinction correction and plasma diagnostics at each spatial element were too cumbersome in the past, especially when computational resources were not readily available. Thus, constant n_e and T_e might be assumed for the extinction correction, and plasma diagnostics were performed subsequently only once to yield constant n_e and T_e even for

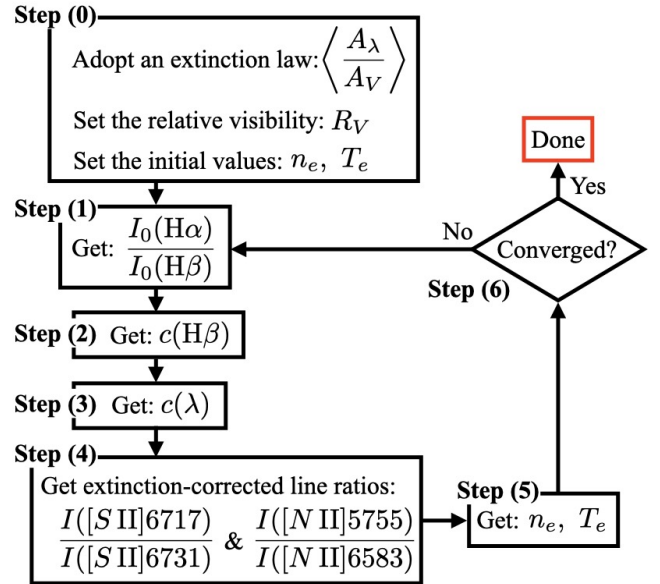


Figure 1. Schematic representation of PPAP, through which $c(\text{H}\beta)$ and $(n_e([\text{S II}], T_e([\text{N II}]))$ are determined by iteration.

extended objects, never to be retroactively checked for consistency. This practice appears to have been adopted for years in the literature. In many of the previous investigations of NGC 6720, a preset T_e was adopted to derive n_e , and then, a preset n_e , instead of the derived n_e , was used to derive T_e , and the computation was left at that (e.g. Lamé & Pogge 1994; Garnett & Dinerstein 2001; O’Dell et al. 2013b), while the subtle intertwined nature of these analyses seems to have been lost in translation.

However, in the present time when decent computational resources are regularly available, there is no reason not to perform iterative searches for $c(\text{H}\beta)$ and (n_e, T_e) at each spatial element through both the extinction determination and plasma diagnostics in a fully self-consistent manner. Therefore, we propose proper plasma analysis practice (PPAP), a fully self-consistent and spatially-resolved procedure of the extinction correction and plasma diagnostics as a streamlined iterative process (schematically represented in Fig. 1):

- (0) Select the extinction law to use and set the R_V value toward the target source as well as the initial n_e and T_e values;
- (1) Compute the theoretical $I_0(\text{H}\alpha)/I_0(\text{H}\beta)$ ratio based on the initial n_e and T_e values following, e.g., Storey & Hummer (1995);
- (2) Compute $c(\text{H}\beta)$ by comparing the observed $I(\text{H}\alpha)/I(\text{H}\beta)$ and theoretical $I_0(\text{H}\alpha)/I_0(\text{H}\beta)$ maps using the PyNeb SETCORR and cHBETA functions (Eq. (2)), and then, $c(\lambda)$ using the PyNeb GETCORR function (Eq. (5)) with the adopted extinction law;

- (3) Correct the observed line flux maps for extinction using the $c(\lambda)$ map obtained in Step (2);
- (4) Determine $n_e([\text{S II}])$ and $T_e([\text{N II}])$ using the extinction-corrected $[\text{S II}]$ 6717-to-6731 Å and $[\text{N II}]$ 5755-to-6583 Å line ratio maps in the PyNeb `GETCROSSTEMDEN` function;
- (5) Compare the old and new $n_e([\text{S II}])$ and $T_e([\text{N II}])$ values, and terminate the process if the convergence is achieved (i.e. the difference is negligible);
- (6) If the convergence condition is not met, repeat Steps (1) through (4) with the new $n_e([\text{S II}])$ and $T_e([\text{N II}])$ values.

When the convergence is achieved at Step (6), the best-fit $c(\text{H}\beta)$, $n_e([\text{S II}])$, and $T_e([\text{N II}])$ distribution maps are left to us for further analyses. The converged $c(\text{H}\beta)$ allows us to produce optimally extinction-corrected line emission maps. With the help of the converged $n_e([\text{S II}])$, and $T_e([\text{N II}])$ maps, extinction-corrected line emission maps in turn yield other products of plasma diagnostics such as ionic and elemental abundance distribution maps. In implementing PPAP for the present study, we employ PyNeb (Luridiana et al. 2015), a python implementation of a set of tools for analyzing emission lines based on the method used by the IRAF NEBULAR package (Shaw & Dufour 1995; Shaw et al. 1998).

3. RESULTS

3.1. The Converged $c(\text{H}\beta)$ Map

3.1.1. Observed Spatial Variations

First and foremost, we examine the converged $c(\text{H}\beta)$ map as the basis for all the subsequent analyses. In Fig. 2, we present the $c(\text{H}\beta)$ map (top) and the corresponding one- σ percent uncertainty map (bottom) of the NW quadrant of NGC 6720 converged via PPAP based on the observed $\text{H}\alpha$ -to- $\text{H}\beta$, $[\text{S II}]$ 6717-to-6731 Å, and $[\text{N II}]$ 5755-to-6583 Å ratio maps. The one- σ uncertainty is calculated at each pixel by varying each of the three input line ratios by its standard deviation ($\pm\sigma_{\text{line ratio}}$) and propagating the resulting uncertainties accordingly. In Fig. 3, we also present the $c(\text{H}\beta)$ radial density distribution. We adopt this format instead of a typical azimuthally-averaged radial profile to better reveal the radial variation of $c(\text{H}\beta)$ itself as well as its spread.

These figures indicate that the converged $c(\text{H}\beta)$ values largely populate the characteristic “main ring” structure of NGC 6720 seen between $\sim 20''$ and $\sim 40''$ from the center slightly elongated along the position angle (PA; E from N) of -120° , but not so much in the central cavity (within $\sim 20''$) and not at all in the region beyond the main ring (beyond $\sim 40''$). Because the effectiveness of PPAP is dictated by the quality of input line emission maps, the whole process can be bottlenecked at Step

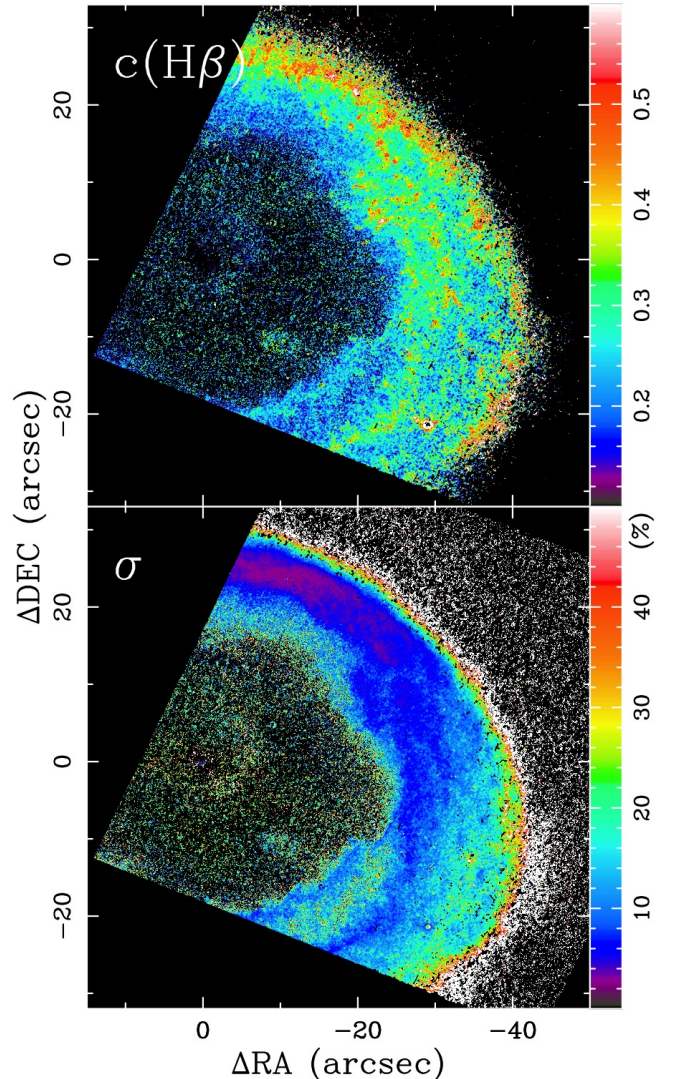


Figure 2. The $c(\text{H}\beta)$ distribution map (top) and the corresponding one- σ percentage uncertainty map (bottom) of the NW quadrant of NGC 6720, derived self-consistently through PPAP. Maps are shown in the original pixel scale of the input *HST* images at $0''.0396 \text{ pix}^{-1}$ with the relative RA and Dec offsets from the position of the central star, (18:53:35.0970, +33:01:44.8831), indicated by the tickmarks. The color wedges show the range of the values presented.

(4) by less sensitive line maps (Fig. 1; § 2.3). For the present case, we do not obtain converged results in all pixels within the inner cavity because S/N of $[\text{S II}]$ line emission is unfortunately marginal (especially Fig. 17c).

Nonetheless, we see that $c(\text{H}\beta)$ is more or less constant at slightly greater than 0.2 over ~ 20 – $25''$ and then increases radially to ~ 0.25 – 0.35 at the outer edge of the main ring (30 – $40''$), with the mean of 0.29 ± 0.09 (corresponding to $\sim 49\%$ attenuation at 4861 Å). At many positions near the outer edge of the main ring, especially along the short axis (PA of -30°), $c(\text{H}\beta)$ is found to be

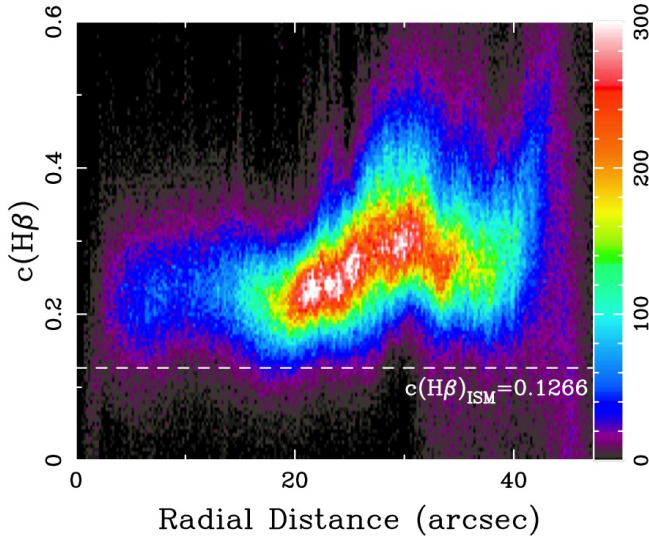


Figure 3. The radial density distribution map of $c(\text{H}\beta)$, with the frequency indicated by the color, showing the $c(\text{H}\beta)$ radial profile without suppressing the azimuthal variation. The ISM contribution to $c(\text{H}\beta)$ (0.1266 ± 0.0007) is marked by the dashed line.

as great as 0.4 or even greater (more than 60% attenuation). On the contrary, the maximum $c(\text{H}\beta)$ at the elongated tip of the main ring along the long axis (PA of -120°) is only marginally high ($\sim 0.25\text{--}0.35$, corresponding to 45–50% attenuation).

This azimuthal trending of $c(\text{H}\beta)$ is generally consistent with the dust distribution in NGC 6720 revealed by far-IR dust continuum emission maps taken with the Herschel Space Observatory (van Hoof et al. 2010). While the spatial resolution differs quite a bit in the optical and in the far-IR, the dust distribution shows a greater degree of dust concentration around the short axis than around the long axis. As suggested, for example, by Guerrero et al. (1997) and O’Dell et al. (2013a), the presence of a denser molecular gas of the photo-dissociation region (PDR) beyond the main ring may be directing outflows emanating from the central region preferentially into the low density polar directions that is slightly inclined with respect to the line of sight, effectively generating the elongated appearance of the main ring (cf. Fig. 14 by Guerrero et al. 1997; Fig. 11 by O’Dell et al. 2013a). Past kinematic studies indeed revealed an expanding ellipsoidal shell whose long-axis is almost aligned with the line of sight (e.g. Guerrero et al. 1997; O’Dell et al. 2007; Martin et al. 2016).

In the central cavity (within $20''$), on the other hand, we find that $c(\text{H}\beta)$ is roughly constant at 0.22 ± 0.06 . The absence of $c(\text{H}\beta)$ near the central star (within $\sim 5''$) does not mean the absence of attenuating dust grains there: $c(\text{H}\beta)$ is simply not reliably computed around the central star because the input line maps are affected by the presence of the central star (e.g. imperfect subtrac-

tion of the continuum). Again, far-IR dust continuum maps show more or less uniform dust emission in the inner cavity (van Hoof et al. 2010), while it is expected that dust grains exist along the line of sight on the near and far sides of the rarefied high-temperature plasma region around the central star.

The observed general radial behavior of $c(\text{H}\beta)$ is consistent with the expected stratification of the nebula. That is, $c(\text{H}\beta)$ values tend to be higher in the main ring where the bulk of the nebula material is located than in the inner cavity where the higher-temperature plasma is rarefied. Then, the radially increasing $c(\text{H}\beta)$ is naturally explained by the radial decrease of the gas temperature, i.e., the degree of ionization.

The present $c(\text{H}\beta)$ map at the exquisite $0''.0396 \text{ pix}^{-1}$ scale (Fig. 2) successfully reveals details of its spatial distribution. A comparison between the $c(\text{H}\beta)$ map and the observed $\text{H}\alpha$ -to- $\text{H}\beta$ map (Fig. 4, top) clearly indicates that the presence of dust grains attenuates the bluer $\text{H}\beta$ line emission more than the redder $\text{H}\alpha$ line emission, leaving a higher $\text{H}\alpha$ -to- $\text{H}\beta$ ratio at that location. Such high $c(\text{H}\beta)$ (high $\text{H}\alpha$ -to- $\text{H}\beta$ ratio) regions appear to form micro-structures that resemble radial cometary structures and/or Rayleigh-Taylor (RT) instability fingers as observed in the Helix Nebula (O’Dell & Handron 1996) and the Crab Nebula (Hester 2008), respectively. There is a greater number of such clumps closer to the outer edge of the main ring. This is probably caused by the inhomogeneous gas distribution in the main ring being eroded by photoevaporating radiation from the central star. Ionizing radiation does not just simply travel radially in the nebula, but permeates through the inhomogeneous gas by going preferentially into low density regions, leaving high-density clumps behind.

As discussed at the end of § 2.3.1, we expect $c(\text{H}\beta)$ of 0.1266 ± 0.007 from the ISM alone. How the converged $c(\text{H}\beta)$ compares with this expectation is demonstrated well in Fig. 3: the ISM component is represented by the horizontal dashed line. We immediately see that the derived $c(\text{H}\beta)$ is greater than the ISM value for the entire extent of the nebula where we have measurements. This result indeed proves that NGC 6720 itself provides the source of self-attenuation in its circumstellar nebula. The circumstellar $c(\text{H}\beta)$ is about 0.1 in the inner cavity ($\sim 20\%$ reduction), as high as 0.3 at the outer edge in the short axis direction ($\sim 50\%$ reduction), and 0.12–0.17 at the outer edge in the long axis direction ($\sim 30\%$ reduction). Hence, the circumstellar contribution to $c(\text{H}\beta)$ in NGC 6720 amounts to about the same or even greater than the ISM contribution. Given that NGC 6720 is an object at a moderate Galactic latitude reasonably away from the Bulge ($(l, b) = (+63.1701, +13.9781)$), it may not be very appropriate, in general, to adopt the ISM $c(\text{H}\beta)$ value indiscriminately as the total $c(\text{H}\beta)$ for any target source.

The circumstellar $c(\text{H}\beta)$ component of ~ 0.1 measured in the inner cavity is most likely attributed to dust grains

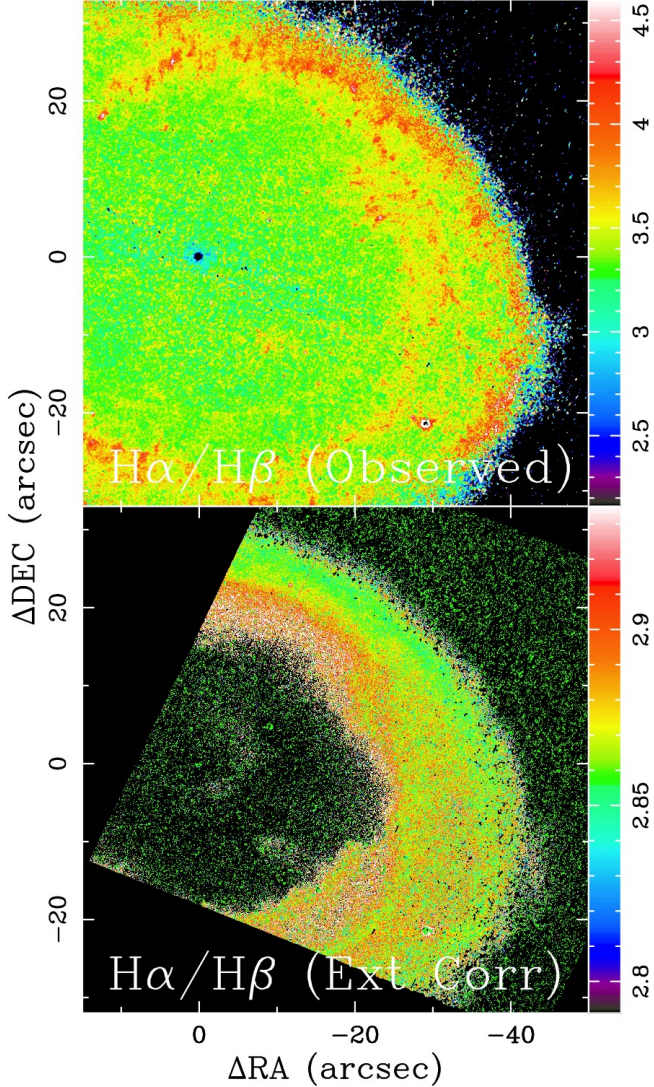


Figure 4. The observed (top) and extinction-corrected (bottom) $H\alpha$ -to- $H\beta$ line ratio maps of the NW quadrant of NGC 6720. Image conventions follow those of Fig. 2. The color wedge shows values in the $\pm 3\sigma$ range around the median.

floating *in front of* the central high-temperature region around the central star along the line of sight. Thus, we expect that there is another $c(H\beta) \sim 0.1$ worth of dust grains *behind* the central high-temperature region. If so, $c(H\beta)$ in the inner cavity as a whole would be about 0.33 including the ISM component ($= 0.13 + 0.1 + 0.1$), which is very much consistent with the amount of $c(H\beta)$ we observe at the outer edge of the main ring. Hence, it appears that the main ring of NGC 6720 contain on average $c(H\beta) \sim 0.2$ worth of dust grains in any radial direction.

3.1.2. Comparison with the Previous Results

One of the first spectral imaging investigation of NGC 6720 was performed by [Lame & Pogge \(1994\)](#) with a Fabry-Perot imaging spectrograph. They presented the observed $H\alpha$ -to- $H\beta$ map (their Fig. 3) and noted a smooth radial increase of the value from 3.68 in the central cavity to 3.74 in the main ring, with the maximum of ~ 3.93 happening at around the 3/4 of the ring (with the median of 3.74 ± 0.22). These values compare reasonably well (within $\sim 10\%$) with what we see in our QP-processed (observed, but line contamination corrected) $H\alpha$ -to- $H\beta$ map (Fig. 4, top), in which the ratio rises from 3.36 ± 0.11 in the central cavity to 3.61 ± 0.12 in the main ring with the median of 3.38 ± 0.40 .

[Lame & Pogge \(1994\)](#) went on to correct for extinction by assuming the constant theoretical $H\alpha$ -to- $H\beta$ ratio of 2.86 in the main ring, for which n_e of 10^2 cm^{-3} and T_e of 10^4 K are assumed via [Hummer & Storey 1987](#) under the same CCM extinction law. This prompted the corrected $H\alpha$ -to- $H\beta$ ratio of 2.81 in the central cavity, which corresponds to T_e of 13,500 K. They attributed the T_e discrepancy to the local inhomogeneity and deviation from the Case B condition, and moved on without re-evaluating the theoretical $H\alpha$ -to- $H\beta$ ratio based on the updated T_e , never seeking consistency between the extinction correction and plasma diagnostics (very typical in the literature). So, their $c(H\beta)$ values would have been 0.31–0.32, which are $\sim 20\%$ greater than ours.

In our case, on the other hand, $c(H\beta)$, n_e , and T_e are iteratively updated for convergence, and our extinction-corrected $H\alpha$ -to- $H\beta$ map (Fig. 4, bottom) yields the mean ratio of 2.863 ± 0.024 in the main ring out of the initial value of 2.858 (and the corresponding derived $n_e([S \text{ II}])$ and $T_e([N \text{ II}])$ maps from the initially assumed 10^3 cm^{-3} and 10^4 K ; see § 3.2), maintaining self-consistency in every single pixel (Fig. 8a). This means that the 20% discrepancy in the analyses by [Lame & Pogge \(1994\)](#) arose because (1) a *uniform* theoretical $H\alpha$ -to- $H\beta$ ratio was imposed across the entire nebula and (2) convergence was not sought among $c(H\beta)$, n_e , and T_e by iteration, i.e., $c(H\beta)$, via the theoretical $H\alpha$ -to- $H\beta$ ratio, was never updated even when n_e and T_e varied.

The same *HST*/WFC3 data set was previously analyzed by [O’Dell et al. \(2013b\)](#). They originally reported radially decreasing $c(H\beta)$ along both the long- and short-axis of the nebula. We communicated with them about this discrepancy during the early phase of writing of this manuscript. It turned out that one of the coefficients in their flux calibration formula for F656N was in error, and that their updated results now show radially increasing $c(H\beta)$ around 0.3 in the main ring ([O’Dell et al. 2021](#)). We note that their derivation is based on the constant $H\alpha$ -to- $H\beta$ ratio of 2.87 across the nebula assuming a 10^4 K gas at low density (the value unspecified) under the extinction law by [Whitford \(1958\)](#) with $R_V = 3.1$. Also, their WFC3 image flux calibration does not follow the standard STScI method,

but is based on their own method established with their own *ground-based* long-slit spectroscopy data (i.e. not generally reproducible).

Other previous analyses were typically based on multi-position-aperture or long-slit spectroscopy (e.g. Hawley & Miller 1977; Barker 1980; Guerrero et al. 1997; Garnett & Dinerstein 2001). Each of these studies adopted a certain extinction law (plus R_V) and theoretical $H\alpha$ -to- $H\beta$ ratio based on their own assumptions of n_e and T_e . The adopted parameters are sometimes explicitly mentioned, and sometimes not. The reported $c(H\beta)$ (plus n_e and T_e) values are generally consistent with our values, some more so and others less. The direct comparisons to assess details beyond general agreement do not seem instructive, as none of the previous derivations were done self-consistently. There is more recent spectral imaging study of NGC 6720 (Martin et al. 2016) based on observations with an imaging Fourier transform spectrometer (Drissen et al. 2019). However, their study is focused on the velocity structure of the nebula, and no plasma diagnostics are discussed.

In light of the previous studies smothered with inconsistencies, the lesson to be learned here seems rather obvious. We ought to eliminate inconsistencies where we can, because any inconsistencies introduced will exacerbate uncertainties in the outcomes. All things considered, we can reiterate one major advantage of PPAP in comparison with other methods in the literature. PPAP yields the self-consistent $c(H\beta)$ (and hence, n_e , and T_e) distribution based on only the input line flux maps plus the choice of the extinction law to adopt, with no need to adopt any other parameters and *ad hoc* assumptions.

3.2. The Converged $n_e([S II])$ and $T_e([N II])$ Maps

3.2.1. Observed Spatial Variations

The $n_e([S II])$ and $T_e([N II])$ distribution maps converged via PPAP are summarized in Fig. 5 with their corresponding percentage uncertainty maps. The radial density distribution maps of $n_e([S II])$ and $T_e([N II])$ are also presented in Fig. 6. In computing $n_e([S II])$ and $T_e([N II])$ with PyNeb (Luridiana et al. 2015), we use the transition probabilities (Einstein As) by Rynkun et al. (2019) and Fischer & Tachiev (2004), and collision strengths by Tayal & Zatsarinny (2010) and Tayal (2011), respectively. The $n_e([S II])$ and $T_e([N II])$ uncertainties are computed in the same way as the $c(H\beta)$ uncertainties. As is the case for $c(H\beta)$, $n_e([S II])$ and $T_e([N II])$ are reliably determined mostly in the main ring. This is partly because of S/N in the diagnostic $[S II]$ line ratio map (Fig. 17), but also partly because the $[S II]$ and $[N II]$ diagnostics are better suited to probe the moderately ionized region (i.e. the main ring) than the highly ionized wind bubble region (i.e. the inner cavity).

The converged $n_e([S II])$ and $T_e([N II])$ maps show a lesser degree of spatial variation in the main ring than the converged $c(H\beta)$ map: we do not recognize micro-

structures in the $n_e([S II])$ and $T_e([N II])$ maps as in the $c(H\beta)$ map. Closer examination suggests that there is some anti-correlation between $n_e([S II])$ and $c(H\beta)$: $n_e([S II])$ tends to be smaller where $c(H\beta)$ is larger. This is indeed expected because dust grains are more likely found where temperature is low, i.e., the degree of ionization is low, and vice versa.

The main ring appears to be divided into the following two parts in terms of $n_e([S II])$ and $T_e([N II])$: (1) the inner part (~ 20 – $25''$), in which both $n_e([S II])$ and $T_e([N II])$ show a radially increasing trend with relatively higher uncertainties ($\sim 25\%$), and (2) the outer part (beyond $25''$ up to 30 – $40''$), where $n_e([S II])$ decreases and $T_e([N II])$ is more or less uniform.

The $n_e([S II])$ and $T_e([N II])$ values increase radially from $\sim 1,000 \text{ cm}^{-3}$ to $\sim 1500 \text{ cm}^{-3}$ in $n_e([S II])$ (with the mean of $1,400 \pm 580 \text{ cm}^{-3}$) and from $\sim 7,000 \text{ K}$ to $\sim 9,300 \text{ K}$ in $T_e([N II])$ (with the mean of $8,390 \pm 1,270 \text{ K}$) in the inner part of the main ring. Their spatial distribution of $n_e([S II])$ and $T_e([N II])$ indicates that this inner part is rather circular in projection (extends up to $\sim 25''$ in all azimuthal directions). Thus, this region is possibly spherical in 3-D, suggesting that this ‘‘spherical’’ region represents the highly-ionized central wind bubble caused by the radiation from the central star, eating its way into the higher density ellipsoidal wind shell (the outer part beyond $\sim 25''$).

Thus, the observed radial rise of $n_e([S II])$ in the inner part of the main ring can be understood as caused by the snowplowing effect by the PN fast wind emanating from the central star (e.g. Kwok 2000). However, the observed radial rise of $T_e([N II])$ may be counter-intuitive. Such radially increasing $T_e([N II])$ trending is recognized numerically, and attributed to the self-shielding effect of the ionizing radiation field: soft ionizing photons are already absorbed by metals in the inner part and remaining hard ionizing photons in the outer part would yield more heat per ionization, making $T_e([N II])$ higher at greater radial distance away from the central star (Kewley et al. 2019).

In the outer part of the ring, $n_e([S II])$ radially decreased to about $1,000 \text{ cm}^{-3}$ (with the mean of $1,170 \pm 540 \text{ cm}^{-3}$), while $T_e([N II])$ remains about the same at $\sim 9,300 \text{ K}$ (with the mean of $9,290 \pm 1,060 \text{ K}$). Given that the degree of ionization is more or less the same in this part of the shell as implied from rather uniform $T_e([N II])$, the radial fall-off of $n_e([S II])$ probably reflects the density distribution in this part.

Azimuthally, $n_e([S II])$ and $T_e([N II])$ change from $\sim 1,500 \text{ cm}^{-3}$ and $\sim 10,500 \text{ K}$ along the short axis to $\sim 500 \text{ cm}^{-3}$ and $T_e([N II]) \sim 8,100 \text{ K}$ along the long axis, respectively. This azimuthal trending is consistent with what we see in the $c(H\beta)$ distribution (Fig. 2). Generally speaking, this azimuthal variation is what gives the observed spread of the $n_e([S II])$ and $T_e([N II])$ values – about $1,000 \text{ cm}^{-3}$ for $n_e([S II])$ and about $2,000 \text{ K}$ for $T_e([N II])$ – in the density distribution (Fig. 6).

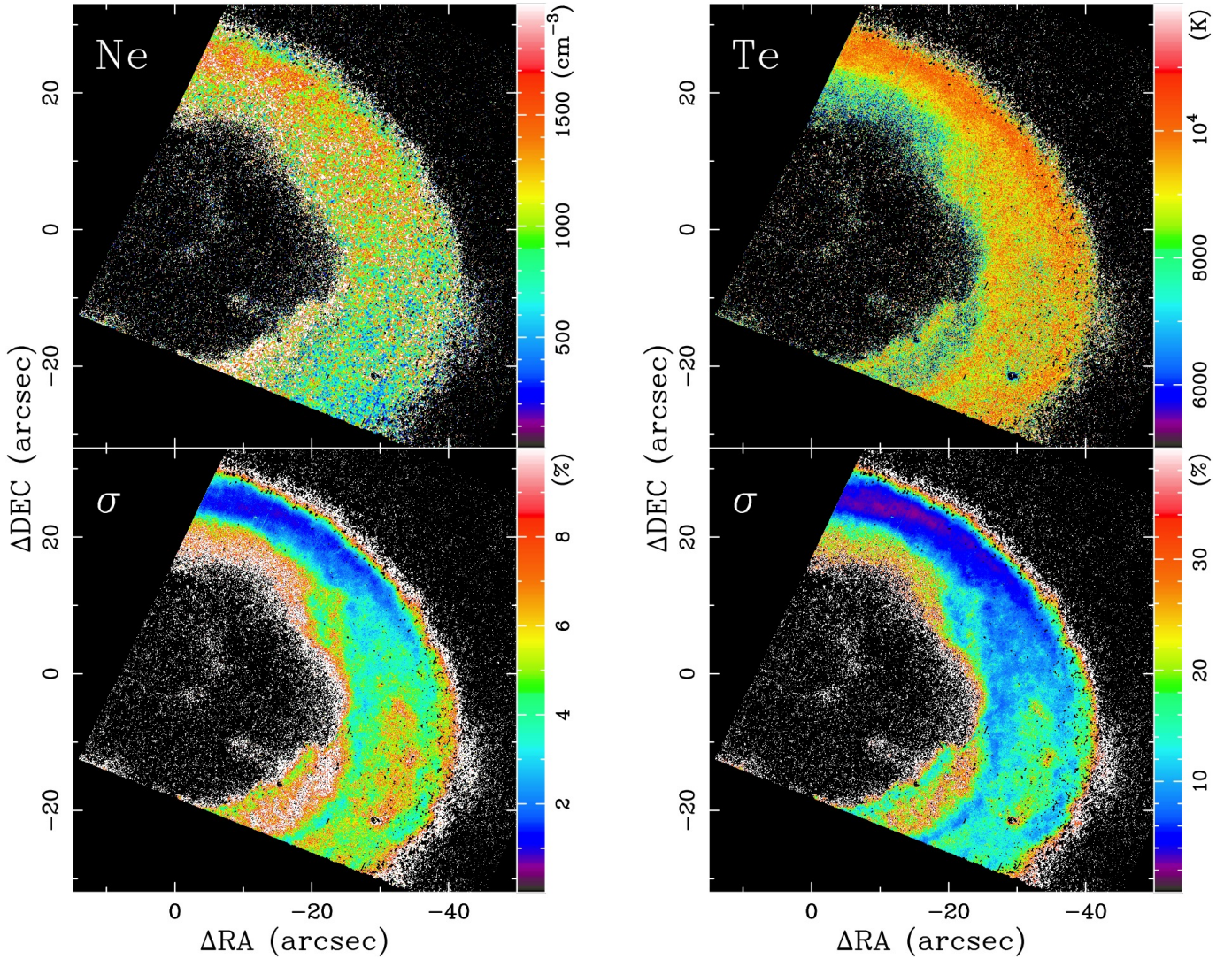


Figure 5. The $n_e([\text{S II}])$ and $T_e([\text{N II}])$ distribution maps with the corresponding one- σ percent uncertainty map derived self-consistently through PPAP (left and right, respectively). Image conventions follow those of Fig. 2.

While the radial density distribution maps do not show any representative $n_e([\text{S II}])$ and $T_e([\text{N II}])$ values in the inner cavity (Fig. 6) as in $c(\text{H}\beta)$ (Fig. 2), the mean $n_e([\text{S II}])$ and $T_e([\text{N II}])$ values nevertheless turn out to be $1,340 \pm 750 \text{ cm}^{-3}$ and $8,140 \pm 1,730 \text{ K}$. Here, readers are reminded that these values are based on the $[\text{S II}]$ and $[\text{N II}]$ diagnostics, which are suited to probe a low-excitation gas. In other words, these measurements are obtained from the low-excitation plasma that lies along the line of sight to the inner cavity, i.e., $[\text{S II}]$ and $[\text{N II}]$ are most likely not co-spatial with the central wind bubble region. Rather, the valid $n_e([\text{S II}])$ and $T_e([\text{N II}])$ values in this region most likely sample the near-side of the thinned-out bipolar cavities of the ellipsoidal shell of the nebula (cf. Fig. 14 by Guerrero et al. 1997; Fig. 11 by O’Dell et al. 2013a).

3.2.2. Comparison with the Previous Results

The previous n_e estimates yielded $500\text{--}700 \text{ cm}^{-3}$ (Lame & Pogge 1994), $470\text{--}615 \text{ cm}^{-3}$ (Guerrero et al. 1997), $660\text{--}740 \text{ cm}^{-3}$ (Garnett & Dinerstein 2001), and $350\text{--}550 \text{ cm}^{-3}$ (O’Dell et al. 2013b), based on the assumed T_e value of 10^4 K and assumed theoretical $\text{H}\alpha$ -to- $\text{H}\beta$ ratio (for which certain n_e was assumed). They used the derived n_e values to update T_e that ranged roughly from 10,000 to 13,000 K, but without updating the theoretical $\text{H}\alpha$ -to- $\text{H}\beta$ ratio (hence, extinction correction) according to the updated n_e and T_e .

More specifically, for example, Lame & Pogge (1994) adopted the theoretical $\text{H}\alpha$ -to- $\text{H}\beta$ ratio of 2.86 uniformly across the nebula, assuming a uniform n_e of 10^3 cm^{-3} and T_e of 10^4 K . A comparison between the assumed theoretical $\text{H}\alpha$ -to- $\text{H}\beta$ ratio of 2.86 and the observed $\text{H}\alpha$ -to- $\text{H}\beta$ ratio of ~ 3.74 yielded a certain $c(\text{H}\beta)$ distribution. Then, extinction corrected $[\text{S II}]$ and $[\text{N II}]$ diagnostic line ratios yielded the $n_e([\text{S II}])$ distribution

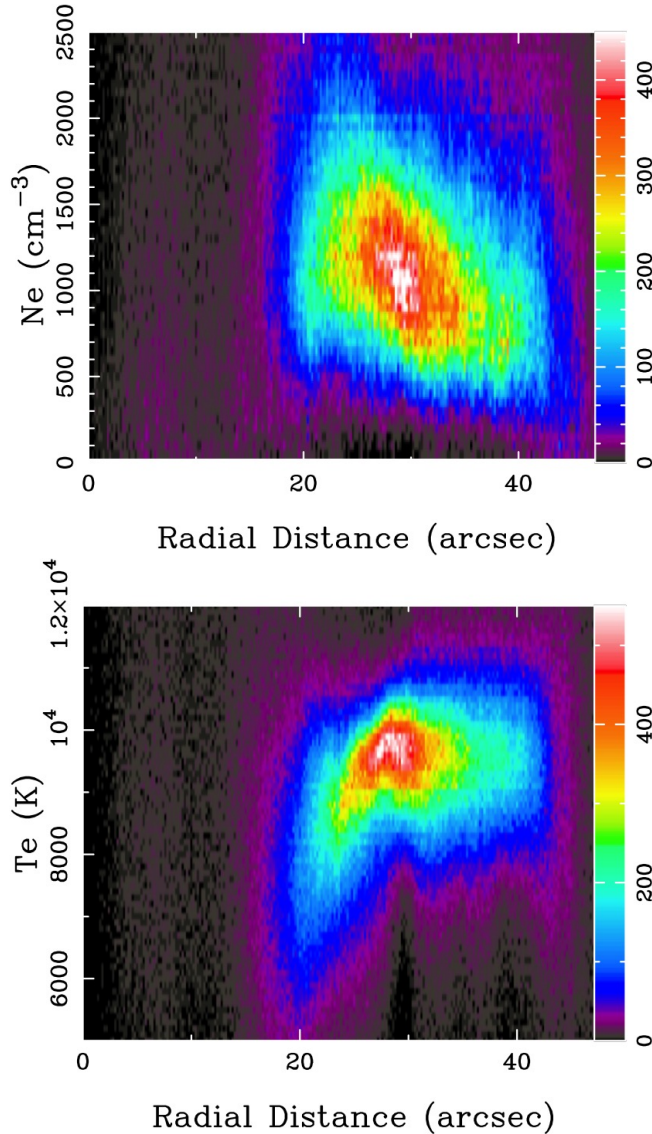


Figure 6. The radial density distribution map of n_e ([S II]) and T_e ([N II]) with the frequency indicated by the color (top and bottom, respectively). Image conventions follow those of Fig. 3.

of $500\text{--}700\text{ cm}^{-3}$ and T_e ([N II]) distribution of $10,000\text{--}13,500\text{ K}$. *Lame & Pogge (1994)* concluded their analyses then, without re-evaluating $c(\text{H}\beta)$ via the updated theoretical $\text{H}\alpha$ -to- $\text{H}\beta$ ratio based on the derived n_e ([S II]) and T_e ([N II]) distributions, which differ from the assumed uniform n_e and T_e , and following through the rest of the analyses for consistency.

Because both of the n_e ([S II]) and T_e ([N II]) distributions were different from the initial uniform assumption, the theoretical $\text{H}\alpha$ -to- $\text{H}\beta$ ratio, and hence, the $c(\text{H}\beta)$ distribution should have had been recomputed for consistency. Subsequently, the resulting n_e ([S II]) and T_e ([N II]) distributions should have had been updated again to reflect changes in the diagnostic line ratios be-

cause of the $c(\text{H}\beta)$ offsets. Ideally, this iteration should have had been repeated until all values converged to the final values for the maximum consistency. Unfortunately, consistency among these parameters was not sought iteratively by *Lame & Pogge (1994)*.

This is very representative of how analyses were performed in the literature. Hence, there does not seem much point in directly comparing the n_e and T_e values found in the literature with our results. The reciprocal dependence among $c(\text{H}\beta)$ and (n_e, T_e) were not considered carefully enough for consistency in the past. The strangest thing in the literature is that inconsistencies in the final $c(\text{H}\beta)$ and (n_e, T_e) values and their derivatives were usually attributed to local inhomogeneities, even though a uniform distribution of the initial parameters were usually assumed to begin with. It is really this initial assumption of uniformity that imposes inconsistencies in the first place. There is really no need to assume $c(\text{H}\beta)$ and (n_e, T_e) : all can be determined simultaneously by seeking convergence iteratively. In the present analyses, only a few iterations (at most 5) were enough.

3.2.3. Tolerable Uncertainties

To make PPAP work effectively, it is important to keep self-consistency in the whole of the analyses. However, at some point, the propagated uncertainties from the line fluxes themselves would become greater than the uncertainties caused by assuming constant (n_e, T_e) . Then, what uncertainties are tolerable in following PPAP? While this question may sound simple, it is actually not simple at all. This is because the tolerable levels of uncertainties are actually dependent on the actual line ratios used, the (n_e, T_e) values themselves, and how varying n_e and T_e are in the actual spatial distribution in the target source, among other things.

For the case of NGC 6720, the n_e and T_e values are spread around $1,340\text{ cm}^{-3}$ and $8,140\text{ K}$ with a width of 750 cm^{-3} and $1,730\text{ K}$, respectively (§ 3.2.1). Thus, if uncertainties in n_e and T_e exceed these spreads, assuming constant (n_e, T_e) would be as good as PPAP. A set of experiments with PyNeb reveal that uncertainties of 10–15% in the [S II] ratio would cause large enough uncertainties in the resulting n_e so that considering non-uniform n_e would not be so meaningful. The same is said for T_e if uncertainties in the [N II] ratio are 25–30%. Hence, uncertainties of roughly 10% and 25–30% can be tolerated in the [S II] and [N II] line flux measurements, respectively. While it is difficult to generalize this result for a particular source, uncertainties of 10% or better appear to be necessary for PPAP to work as a rule of thumb.

3.3. Gas-to-Dust Ratio Map

With the $c(\text{H}\beta)$ and $(n_e$ ([S II]), T_e ([N II])) maps determined, it is possible to evaluate the gas-to-dust mass

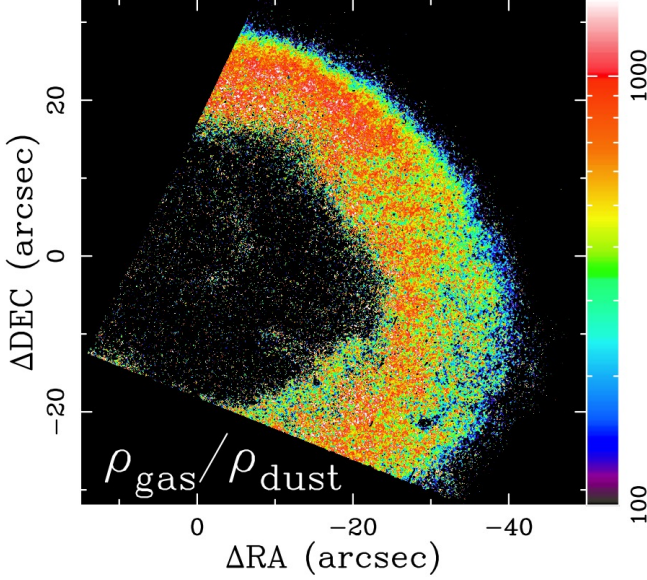


Figure 7. The gas-to-dust mass ratio map at H β obtained from the extinction-corrected H β , (n_e ([S II]), T_e ([N II])), and c (H β) maps by assuming certain dust properties. Image conventions follow those of Fig. 2.

ratio map at H β . This is because dust grains are represented by c (H β), while H β -emitting ionized gas is represented by the H β surface brightness map, n_e ([S II]) map, and the H β emissivity map derived from the (n_e ([S II]), T_e ([N II])) maps. The definition of the extinction allows us to relate c (H β) and the gas-to-dust mass ratio as follows.

$$\begin{aligned} c(\text{H}\beta) &= \frac{A_{\text{H}\beta}}{2.5} = (\log e)\tau_{\text{H}\beta} \\ &= (\log e)(Q_{\text{H}\beta}^{\text{ext}}\pi a^2)N_{\text{dust}} \\ &= (\log e)(Q_{\text{H}\beta}^{\text{ext}}\pi a^2)\frac{\rho_{\text{dust}}/m_{\text{dust}}}{\rho_{\text{H}^+}/m_{\text{H}^+}}N_{\text{H}^+} \end{aligned} \quad (6)$$

where $N_{[\text{dust}, \text{N}^+]}$, $\rho_{[\text{dust}, \text{N}^]}$, and $m_{[\text{dust}, \text{N}^]}$ are the column density, mass density, and particle mass of dust grains and H β -emitting gas, respectively, and $Q_{\text{H}\beta}^{\text{ext}}$ is the extinction efficiency coefficient under the assumption of grains being spheres of radius a . Hence, the gas-to-dust mass ratio is;

$$\begin{aligned} \frac{\rho_{\text{H}^+}}{\rho_{\text{dust}}} &= (\log e)(Q_{\text{H}\beta}^{\text{ext}}\pi a^2)\frac{m_{\text{H}^+}}{m_{\text{dust}}}\frac{N_{\text{H}^+}}{c(\text{H}\beta)} \\ &= (\log e)(Q_{\text{H}\beta}^{\text{ext}}\pi a^2)\frac{m_{\text{H}^+}}{\frac{4\pi}{3}a^3\rho_{\text{dust}}^{\text{bulk}}}\frac{N_{\text{H}^+}}{c(\text{H}\beta)} \\ &= \frac{3(\log e)Q_{\text{H}\beta}^{\text{ext}}m_{\text{H}^+}}{4a\rho_{\text{dust}}^{\text{bulk}}}\frac{N_{\text{H}^+}}{c(\text{H}\beta)} \end{aligned} \quad (7)$$

where $\rho_{\text{dust}}^{\text{bulk}}$ is the bulk density of dust grain material.

Meanwhile, the H β surface brightness is expressed in terms of the column density of H β -emitting gas as fol-

lows.

$$\begin{aligned} I_{\text{H}\beta} &= \int \frac{\epsilon_{\text{H}\beta}n_en_{\text{H}^+}}{4\pi}ds \\ &\approx \frac{\epsilon_{\text{H}\beta}n_e}{4\pi} \int n_{\text{H}^+}ds = \frac{\epsilon_{\text{H}\beta}n_e}{4\pi}N_{\text{H}^+} \end{aligned} \quad (8)$$

where the integral is done through the target along the line of sight, $\epsilon_{\text{H}\beta}$ is the H β emissivity as defined by Storey & Hummer (1995) as a function of n_e ([S II]) and T_e ([N II]). By combining the above two equations, we have

$$\frac{\rho_{\text{H}^+}}{\rho_{\text{dust}}} = \frac{3\pi(\log e)Q_{\text{H}\beta}^{\text{ext}}m_{\text{H}^+}}{a\rho_{\text{dust}}^{\text{bulk}}}\frac{I_{\text{H}\beta}}{\epsilon_{\text{H}\beta}n_e c(\text{H}\beta)} \quad (9)$$

Then, we can derive the gas-to-dust mass ratio map at H β using the extinction-corrected H β map (which gives $I_{\text{H}\beta}$), the (n_e ([S II]), T_e ([N II])) maps (which give $\epsilon_{\text{H}\beta}$ and n_e), and the c (H β) maps, by assuming spherical dust grains of “smoothed astronomical silicate” (Weingartner & Draine 2001) of radius 0.1 μm and bulk density 3 g cm $^{-3}$ (as the dust chemistry of NGC 6720 is still unknown).

The derived gas-to-dust mass ratio map at H β is presented in Fig. 7. The distribution appears similar to the n_e ([S II]) map (Fig. 5), with the median of 437 ± 357 , which is a few times greater than the “typical” value of 100. The derived values need to be considered as the lower limit because we take into account only the H β -emitting ionized gas in the main ring, in which some non-negligible amount of atomic H gas component is expected. According to a photoionization model of NGC 6720 by van Hoof et al. (2010), the amount of ionized and neutral (both atomic and molecular) gasses is about the same (they quoted $\log(n_e) = 2.62$ and $\log(n_{\text{H}} = 2.60)$). Thus, we account for only about 50% of the gas. Also, the derived c (H β) includes the ISM contribution, which amounts to at most roughly 50% (Fig. 2).

Therefore, the total gas-to-dust mass ratio seems to be about 1600 in the main ring. Clearly, a “typical” ratio of 100 cannot be used indiscriminately for the circumstellar dust component, especially when the amount of dust component may be reduced because of local environments. In the literature, it is often practiced to estimate N_{H} from $A(V)$ by adopting an old empirical ISM relation, $N_{\text{H}} \approx (1.87 \times 10^{21}) \times A(V)$ (Savage & Mathis 1979). However, this relation implicitly assumes the gas-to-dust mass ratio of 100 for the “average” ISM. Thus, as we demonstrate here, it is simply wrong to adopt such an $A(V)$ -to- N_{H} relation indiscriminately to any object for which some circumsource dust component is expected.

3.4. Extinction-Corrected Line Emission Maps

Fig. 8 shows the extinction-corrected line maps relative to H β extracted from the present *HST*/WFC3 data

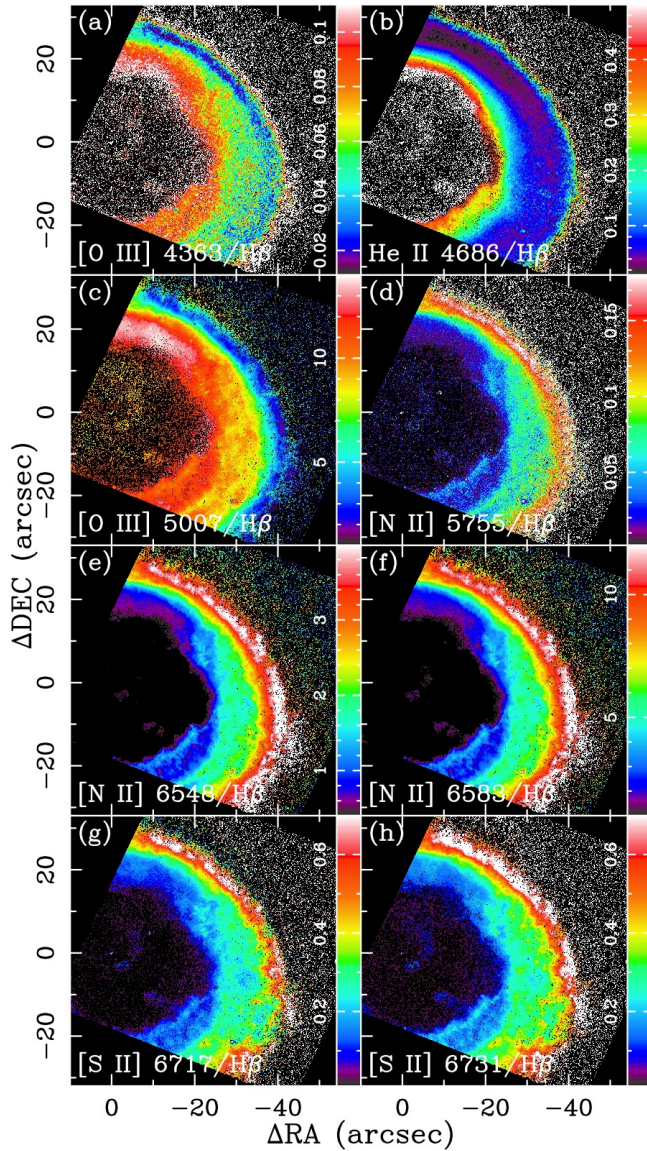


Figure 8. Various extinction-corrected line maps (relative to $H\beta$) of the NW quadrant of NGC 6720: (a) [O III] 4363 Å/ $H\beta$, (b) He II 4686 Å/ $H\beta$, (c) [O III] 5007 Å/ $H\beta$, (d) [N II] 5755 Å/ $H\beta$, (e) [N II] 6548 Å/ $H\beta$, (f) [N II] 6583 Å/ $H\beta$, (g) [S II] 6717 Å/ $H\beta$, and (h) [S II] 6731 Å/ $H\beta$. The wedge on the right in each panel indicates the adopted linear color scale. Image conventions follow from those of Fig. 2.

set. These individual line maps reveal the spatial variation of the relative abundance of specific ionic/elemental species within extended nebulae. Quick inspection of these maps suggests that there are three general patterns of the emission morphology owing to the different excitation levels represented by these lines.

First, a strong circular emission region is seen only in the inner cavity ($< 20''$) as in the He II 4686 Å map (Fig. 8b), as previously reported by *Lame & Pogge (1994)*. This region can be recognized only by the fast

radial decrease of emission around $\sim 20''$. Most likely this region represents the spherical PN wind bubble at the core of the nebula, in which the ambient temperature is the highest.

Second, there is another circular emission region that appears more extended than the He II 4686 Å region, encompassing the inner part of the main ring (up to 25–30''), as seen in the [O III] 4363 and 5007 Å maps (Fig. 8a,c). This region is where the $H\alpha$ -to- $H\beta$ ratio is high (Fig. 4, bottom), and where $c(H\beta)$, n_e , and T_e radially increase to the maximum (Figs. 3 and 6), delineating the extent of the ionized region.

Third, emission is strong only in the periphery of the main ring (beyond $\sim 30''$) as in the [N II] and [S II] maps (Fig. 8d–h). This region corresponds to where $c(H\beta)$ is high (~ 0.3 and above; Figs. 2, 3). $n_e([S II])$ and $T_e([N II])$ are also high in this region ($1,200 \text{ cm}^{-3}$, Figs. 5; $> 10^4 \text{ K}$, 6), most likely representing the PDR surrounding the ionized region.

The apparent transition of morphology from the inner part (radially decreasing) to outer part (radially increasing) of the main ring is quite remarkable. The radially increasing trending of $T_e([N II])$ toward the periphery of the main ring (Fig. 5, right) is promoted by the radially increasing trending of [S II] and [N II] line emission (Figs. 8d–h). As discussed earlier, this is interpreted as the self-shielding effect, in which the majority of the ionizing photons is already consumed in the inner cavity and in the inner part of the main ring and the left-over far-reaching high-energy photons heat the outer part of the main ring. Hence, this transition zone at $\sim 30''$ from the central star very likely corresponds to the location of the ionization front (IF) that separates the high-excitation emission region (Figs. 8a–c) and the low-excitation region (Figs. 8d–h).

Comparisons between two line maps also provide a wealth of information. $H\alpha$ emission is representative of the ionized region, while [N II] emission is of the PDR. Hence, the [N II] 6583 Å-to- $H\alpha$ line ratio map helps to spatially separate these regions (Fig. 9, top), i.e., to identify where IF is located. This is one of the reasons why blending of $H\alpha$ and [N II] lines in the $H\alpha$ band can be a critical issue. IF is most likely located where the [N II] 6583 Å-to- $H\alpha$ gradient becomes the steepest.

The radial density distribution map (Fig. 9, bottom) indicates that the steepest gradient happens at various radii depending on the azimuthal angle. Around the short axis, the ratio remains low in the inner part of the main ring, and precipitously increases at $\sim 25''$. (*Lame & Pogge 1994*) and (*O'Dell et al. 2013a*) noted that the apparent physical thinness of the [N II]-and-[S II]-bright region at the periphery of the main ring (roughly a few arcsec width) indicated that at the line of sight in this region IF intersects nearly at parallel with our line of sight. This means that the inclination of the hollow ellipsoidal shell of the main ring of NGC 6720 (cf. Fig. 14 by *Guerrero et al. 1997*; Fig. 11 by *O'Dell et al. 2013a*)

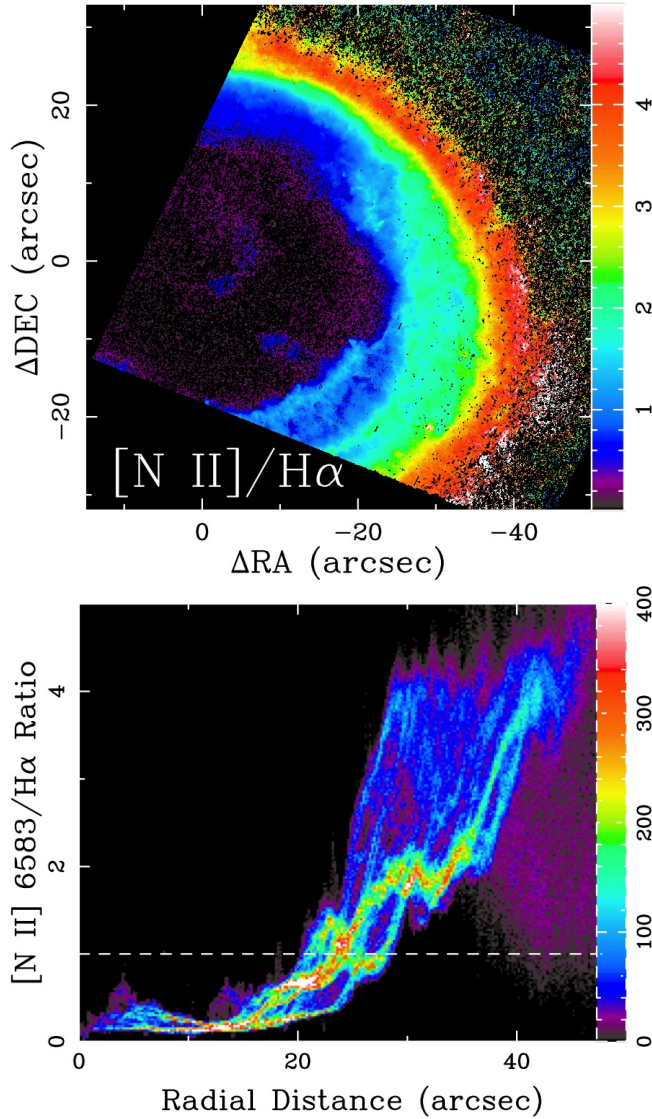


Figure 9. [Top] The [N II] 6583-to- $H\alpha$ line ratio map distinguishes the ionized region (< 1) from the PDR (> 1). Image conventions follow those of Fig. 2. [Bottom] The radial density distribution map of the [N II] 6583-to- $H\alpha$ line ratio shows the IF as the region of the steepest gradient between $20''$ and $40''$. The dashed line is where the ratio is unity.

is pivoted around the short axis in the plane of the sky (Guerrero et al. 1997; O’Dell et al. 2007; Martin et al. 2016). This further means that along the long axis we are looking into the inclined inner wall of the hollow ellipsoidal shell (i.e. IF), where the [N II] 6583 Å-to- $H\alpha$ ratio starts to rise at small radii but increases rather slowly, meandering around 2. This meandering suggests that the IF surface is not necessarily of uniform density and may be sprinkled with micro-structures (e.g. those associated RT/KH instabilities; § 3.1). Hence, the size distribution of these micro-structures, may yield useful

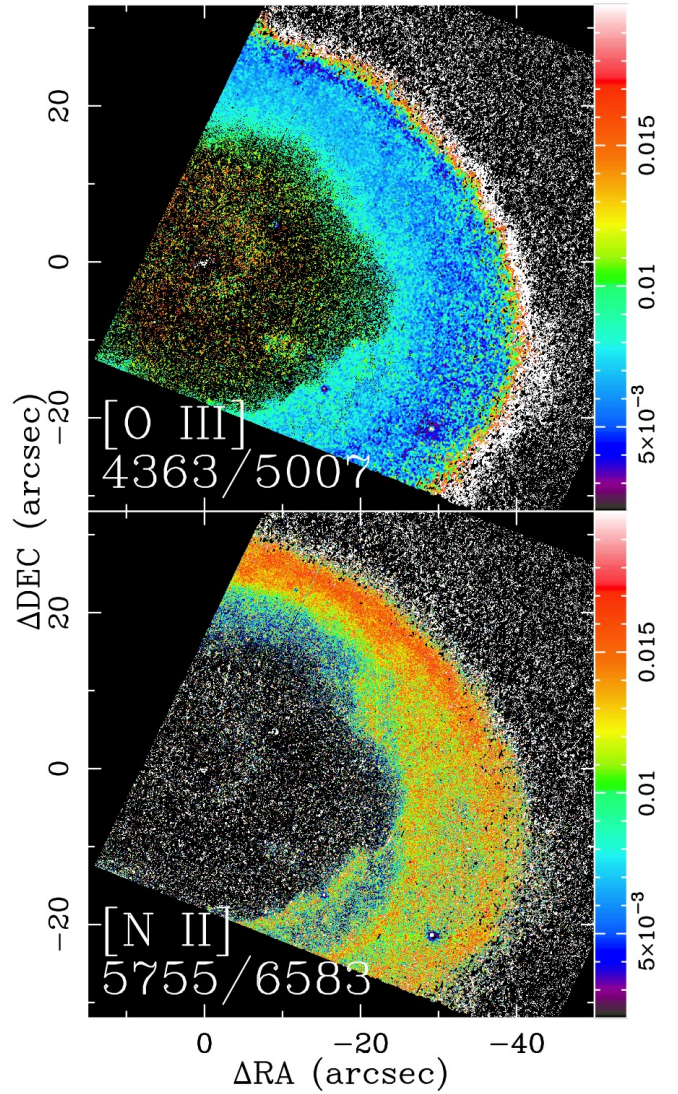


Figure 10. The [O III] 4363-to-5007 Å (top) and [N II] 5755-to-6583 Å (bottom) line ratio maps both compare the spatial distribution of the 1S_0 to 1D_2 transition with that of the 1D_2 to 3P_2 transition, but reveal opposite spatial variations (though the range of ratio is the same as indicated by the color wedge) because of the “ T_e ([N II]) inversion” by self-shielding of ionizing photons. Image conventions follow those of Fig. 2.

constraints for numerical simulations to determine hydrodynamical IF properties.

Another interesting comparison is between the [O III] 4363-to-5007 Å and [N II] 5755-to-6583 Å line ratio maps (Fig. 10). These line ratios compare the 1S_0 to 1D_2 transition with the 1D_2 to 3P_2 transition of the O^{2+} and N^+ ions. The former transition probes higher temperature regions than the latter transition. However, interestingly, these line ratios exhibit opposite trending. The [O III] 4363-to-5007 Å line ratio map (Fig. 10, top) shows larger ratios in the inner region of the main ring than

in the outer region. This is expected from the radially-decreasing general temperature structure of the nebula.

On the other hand, the [N II] 5755-to-6583 Å ratio map (Fig. 10, bottom) shows relatively larger values in the outer region of the main ring than in the inner region. This is exactly the same “ T_e [N II] inversion” in the main ring seen above in § 3.2 (Fig. 5, right) as a consequence of self-shielding of low-energy ionizing radiation by metals in the inner part of the main ring (Kewley et al. 2019).

This comparison plainly demonstrates the importance of adopting diagnostic lines that arise from the very region of interest. The [S II] and [N II] lines probe the same energy regimes, i.e., the resulting n_e [S II] and T_e [N II] would be likely co-spatial. However, the [O III] lines probe higher temperature regimes than the [N II] lines do (i.e., the [O III] lines are more suited to probe the inner cavity). Hence, plasma diagnostics done with the [S II] and [O III] lines would not make much sense as the n_e [S II] and T_e [O III] are not co-spatial, and T_e [O III] most likely exhibits opposite trending with respect to T_e [N II].

3.5. N^+ and S^+ Relative Abundance Maps

The final step of plasma diagnostics is the determination of ionic and elemental abundance distributions. Theoretically, for a given set of n_e and T_e , ionic populations for a particular ionic species should be uniquely determined from any line emission/transition of the adopted N -level system. For the present study, it is natural to compute the ionic abundance distribution maps of $n(N^+)$ and $n(S^+)$ relative to $n(H^+)$ using any of the [N II] and [S II] line maps, as our derivation of n_e and T_e is based on the [N II] and [S II] lines (§ 3.2; Figs. 5, 6).

Here, we use the PyNeb GETIONABUNDANCE function with the extinction-corrected line maps at [N II] 5755 and 6583 Å and [S II] 6717 and 6731 Å (Figs. 8d,f-h). If the resulting relative N^+ and S^+ abundance maps come out to be identical for each of the [N II] and [S II] pairs, we can safely say that the robustness of the proposed PPAP is guaranteed. The results of this experiment are summarized in Fig. 11. The left column shows the $n(N^+)/n(H^+)$ maps (Fig. 11a,b) derived from the [N II] 6583 and 5755 Å line maps (Figs. 8d,f), and their difference in percentage (Fig. 11c). Similarly, the right column presents the same for S^+ from the [N II] 6717 and 6731 Å lines (Figs. 11g,h).

The derived $n(N^+)/n(H^+)$ and $n(S^+)/n(H^+)$ vary from about 5×10^{-5} and 10^{-6} at the inner edge to about 3.2×10^{-4} and 6.3×10^{-6} at the outer edge of the main ring, respectively. These values are consistent with previously determined values at various positions in the nebula presented by Barker (1987) ($n(N^+)/n(H^+)$ of 9.5×10^{-6} to 2.21×10^{-4} from multi-position aperture spectroscopy) and Liu et al. (2004) ($n(N^+)/n(H^+)$ of 6.61×10^{-5} and $n(S^+)/n(H^+)$ of 1.23×10^{-6} based on line intensities for the entire nebula obtained by scan-

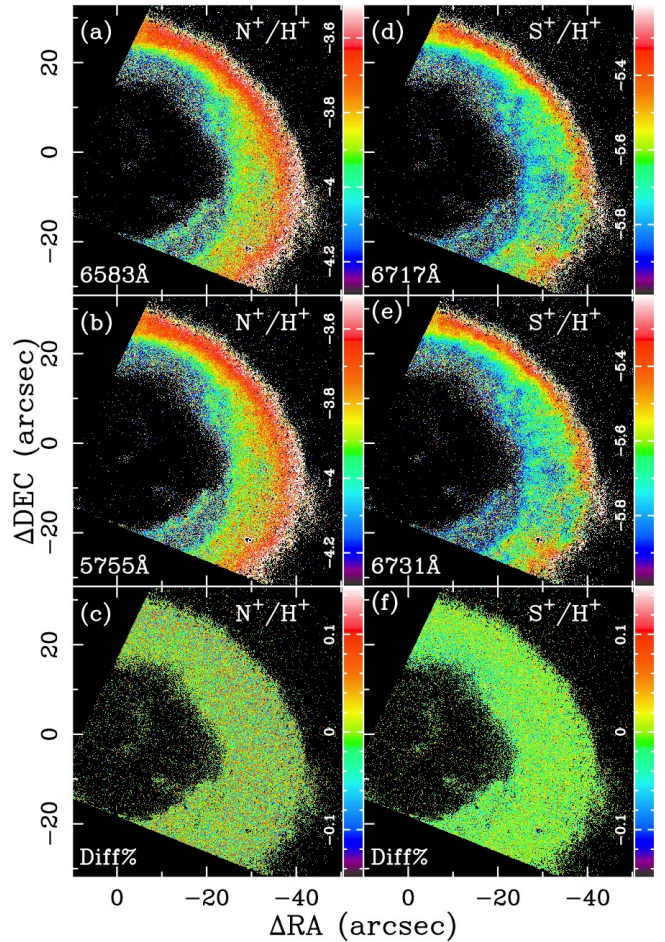


Figure 11. Relative ionic abundance distribution maps of $n(N^+)/n(H^+)$ derived from the (a) [N II] 6583 Å and (b) [N II] 5755 Å lines and (c) their percentage difference map, and of $n(S^+)/n(H^+)$ derived from the (d) [S II] 6717 Å and (e) [S II] 6731 Å lines and (f) their percentage difference maps. These demonstrate that the derived relative ionic abundance maps are identical. The wedge shown in each frame indicates the adopted log color scale from 5×10^{-5} to 3.2×10^{-4} for $n(N^+)$ and from 10^{-6} to 6.3×10^{-6} for $n(S^+)$ for the abundance map and the adopted linear color scale from -0.15% to $+0.15\%$ for the percentage difference maps. Image conventions follow from those of Fig. 2.

ning a long slit across the nebula during exposure), for example. However, readers are reminded that direct comparisons of numerical values do not carry significant weight, as previous analyses were not fully spatially resolved and involved inconsistencies.

What is remarkable here is that the spatial distribution of N^+ and S^+ ions derived from different lines/transitions appears very much identical to each other (Fig. 11a,b for $n(N^+)/n(H^+)$ and Fig. 11d,e for $n(S^+)/n(H^+)$). The percentage difference turns out to be practically nil: $0.0004 \pm 0.053\%$ and $-0.005 \pm$

0.036 % for $n(\text{N}^+)/n(\text{H}^+)$ and $n(\text{S}^+)/n(\text{H}^+)$, respectively (Fig. 11c,f).

We see a greater concentration of N^+ and S^+ ions in the outer part of the main ring. This is expected from the fact that N^+ and S^+ are species of lower excitation energies. Comparing N^+ and S^+ , the lower-excitation S^+ ions are distributed in a physically narrower extent than N^+ ions at the periphery of the main ring. These ionic abundance distribution maps would certainly allow empirical analyses of their spatial variations in more depth, providing excellent constraints for photoionization and PDR models.

In the past, the abundance derivation for a particular ionic species from different lines/transitions usually yielded different results, and their average was adopted as the final abundance value. However, it is not too difficult to understand that one obtains different abundance values from different lines/transitions, given how analyses were typically done, using $n_e([\text{S II}])$ and $T_e([\text{N II}])$ that are not necessarily consistent (discrepancies typically at $\sim 10\%$ or greater) with $c(\text{H}\beta)$ or $\text{H}\alpha$ -to- $\text{H}\beta$, and hence, not necessarily consistent with $n(\text{N}^+)$ and $n(\text{S}^+)$.

Such practice is intolerable in performing plasma diagnostics for extended objects using spectral maps. Here, PPAP is followed diligently, paying particular attention to self-consistency for both the interstellar extinction correction and plasma diagnostics, to yield identical abundances from multiple transitions of the same ionic species. Thus, Fig 11 demonstrates clearly that spatially-resolved plasma diagnostics can be performed as rigorous numerical analyses if we adopt PPAP by seeking a converged self-consistent solution iteratively.

Before concluding this section, we emphasize the importance of self-consistency in abundance analyses from a different perspective. Fig. 12 illustrates how much discrepancy in relative $n(\text{N}^+)/n(\text{H}^+)$ abundance can arise when n_e and T_e values are deviated from the exact solution (set to be 10^3 cm^{-3} and 10^4 K) for diagnostics with the $[\text{N II}] 6583 \text{ \AA}$ (which is known to be temperature diagnostic) and $[\text{N II}] 121 \mu\text{m}$ (which is known to be density diagnostic) lines. The top panel of Fig. 12 shows that deviations of tens of % from the “true” value are possible when $T_e([\text{N II}])$ is altered even with a few hundred K in T_e . Similarly, the bottom panel of Fig. 12 proves discrepancies in tens of % can arise if n_e is varied by only a couple of hundred cm^{-3} .

In the present analyses above, we see that the exact converged/optimized solution for $n_e([\text{S II}])$ ranges from ~ 500 to $\sim 1,500 \text{ cm}^{-3}$ (Fig. 5, left), while $T_e([\text{N II}])$ ranges from $\sim 8,000$ to $\sim 1,1000 \text{ K}$ (Fig. 5, right). The radial density distribution for these values shows at any given radial bin, there is a spread of $\sim 1,000 \text{ cm}^{-3}$ in $n_e([\text{S II}])$ and $\sim 2,000 \text{ K}$ in $T_e([\text{N II}])$ because of the spatial variation in the azimuthal direction (Fig. 6). According to Fig. 12, the $T_e([\text{N II}])$ spread of $\sim 2,000 \text{ K}$ corresponds to -20 to $+30\%$ discrepancy in the resulting N^+ abundance, while the $n_e([\text{S II}])$ spread of

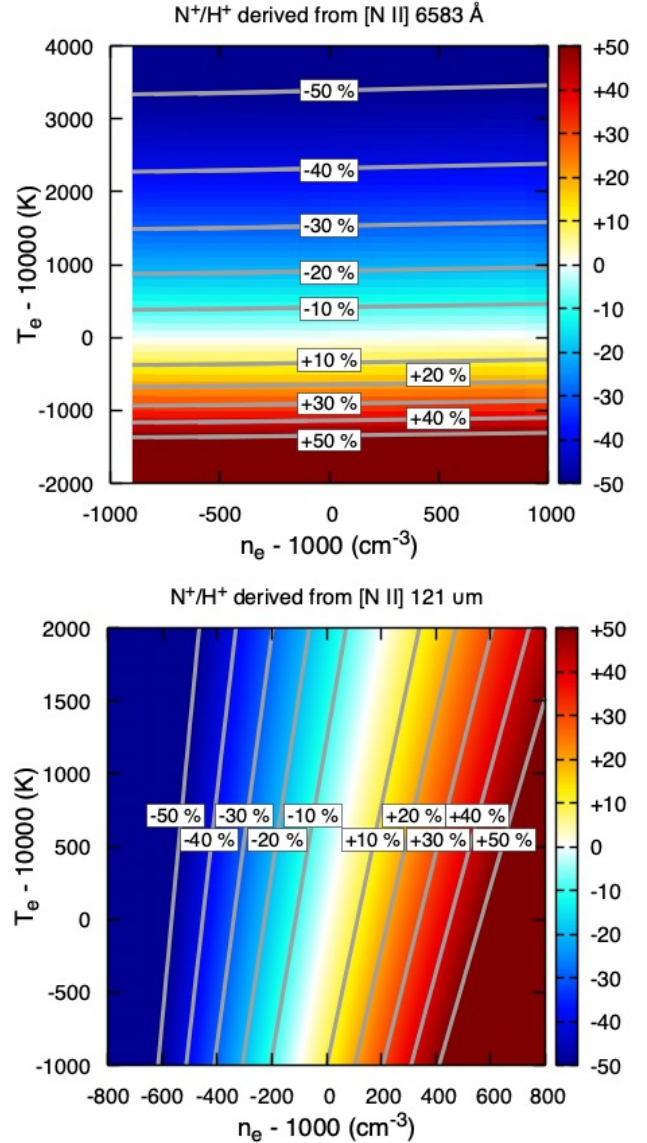


Figure 12. Relative % differences in the $n(\text{N}^+)/n(\text{H}^+)$ abundance when n_e and T_e are deviated from the reference values (of 10^3 cm^{-3} and 10^4 K) based on the $[\text{N II}] 6583 \text{ \AA}$ (top) and $[\text{N II}] 121 \mu\text{m}$ (bottom) diagnostics.

$\sim 1,000 \text{ cm}^{-3}$ corresponds to roughly $\pm 50\%$ discrepancy. Hence, as soon as we allow simplifications and/or rounding of n_e and T_e in the course of extinction correction and plasma diagnostics, we are destined to be compromised by discrepancies at tens of % in the derivatives.

3.6. Overall Quantitative Assessment

We have thus established that the proposed PPAP (1) allows us to perform both the extinction correction and plasma diagnostics as a streamlined single process, and (2) offers more self-consistent and exact solutions of $c(\text{H}\beta)$ and (n_e, T_e) , plus other derivatives, than any of the previous procedures in the literature. The beauty of

PPAP may rest on its straightforwardness, as it is based solely on a set of relevant line emission distribution maps obtained by some spectral mapping observations, with just the initial choice of the extinction law and R_V value to adopt. There is no need to assume anything else.

To reiterate, PPAP is borne out because there is reciprocal, but subtle, dependence of critical parameters between the determination of extinction ($c(\text{H}\beta)$) and plasma diagnostics (n_e and T_e of the same energy regime). That is, $c(\text{H}\beta)$ is necessary to correct observed line emission maps for extinction in order to perform plasma diagnostics, while $c(\text{H}\beta)$ cannot be obtained unless we obtain n_e and T_e by performing plasma diagnostics with extinction-corrected line emission maps. Thus, none of these quantities can be determined independently, and hence, by carefully following through these mutual dependence to the end of the analyses via an iterative search for convergence, we can find $c(\text{H}\beta)$ and (n_e, T_e) that are consistent with each other.

To further demonstrate the robustness of PPAP, here we assess how much improvement is offered by PPAP by quantifying discrepancies that arise by not following PPAP properly. As an example of such a “wrong” practice, first we emulate “typical” plasma diagnostics widely practiced in the literature by adopting the following assumptions and simplifications:

- (1) No QP line extraction
The raw F656N and F658N images are adopted as the $\text{H}\alpha$ and $[\text{N II}]$ 6583 Å line emission maps, respectively. Hence, the adopted $\text{H}\alpha$ and $[\text{N II}]$ 6583 Å line maps are compromised by mutual line contamination.
- (2) Uniform theoretical $\text{H}\alpha$ -to- $\text{H}\beta$ ratio of 2.858
Uniform distribution of n_e at 10^3 cm^{-3} and T_e at 10^4 K is assumed. Then, it follows that the theoretical $\text{H}\alpha$ -to- $\text{H}\beta$ ratio is 2.858 (e.g. Hummer & Storey 1987; Storey & Hummer 1995). Hence, the adopted ratio is applicable only when $n_e = 10^3 \text{ cm}^{-3}$ and $T_e = 10^4 \text{ K}$.
- (3) Simplified $n_e([\text{S II}])$ diagnostic
For an n_e diagnostic using the $[\text{S II}]$ 6717-to-6731 Å line ratio, a simple analytic form of $\log n_e = 4.71 - 2.00 \times I(6717)/I(6731)$ is adopted. This expression reproduces the logistic functional relation between n_e and the $[\text{S II}]$ line ratio fairly well under the assumption of $T_e = 10^4 \text{ K}$ (e.g. Osterbrock & Ferland 2006; O’Dell et al. 2013b). Hence, if the true T_e deviates from 10^4 K , the relation would not yield correct $n_e([\text{S II}])$.
- (4) Simplified $T_e([\text{N II}])$ diagnostic
For a T_e diagnostic using the $[\text{N II}]$ the 5755-to-6583 Å line ratio, an analytic expression of $I(5755)/I(6583) = 5.17 \exp(2.5 \times 10^4/T_e)/(1 + 2.5 \times T_e^{-1/2})$ is adopted. This is an approximated function that relates T_e to the $[\text{N II}]$ line

ratio under the assumption of $N_e = 10^3 \text{ cm}^{-3}$ (e.g. Osterbrock & Ferland 2006; Pradhan & Narhar 2015). Hence, if the true n_e deviates from 10^3 cm^{-3} , the relation would not yield correct $T_e([\text{N II}])$.

In short, in this example, the assumption of uniform $n_e([\text{S II}])$ of 10^3 cm^{-3} and $T_e([\text{N II}])$ of 10^4 K is forced, and the issue of line contamination is not properly mitigated. Hence, unless uniform n_e and T_e come out from PPAP as assumed, the results of the analyses have to be regarded as suspect because inconsistencies between the initial assumptions and the outcomes are not resolved.

As another example of a “wrong” practice, we perform PPAP only partially, by omitting both or either one of the two components of PPAP: the QP line extraction and iterative search for convergence. We can then quantify how much discrepancies can arise in the end by failing to remove line contamination and/or leaving inconsistencies among the reciprocally dependent critical parameters in the problem.

The resulting discrepancies from all of these trial cases are graphically presented in Fig. 13 as relative percentage difference distribution maps. For $c(\text{H}\beta)$ and (n_e, T_e), the outcomes from the “wrong” analyses are compared with the results from full PPAP (§ 3.1, § 3.2). For the N^+ and S^+ abundances, a comparison is made between the resulting two abundance maps obtained from the adopted two diagnostic lines individually (§ 3.5). The mean and standard deviation of the distribution of the relative percentages are also summarized in Table 2.

In general, n_e and T_e anti-correlate with the theoretical $\text{H}\alpha$ -to- $\text{H}\beta$ line ratio, and hence, $c(\text{H}\beta)$. This is rather intuitive as the presence of attenuating dust grains (higher $c(\text{H}\beta)$) suggests more contrasted $\text{H}\alpha$ -to- $\text{H}\beta$ line ratios and lower degrees of ionization (lower n_e and T_e). However, when iterative adjustment of $c(\text{H}\beta)$ and (n_e, T_e) are not performed, the initial assumption of (n_e, T_e), i.e., how they differ from the true (n_e, T_e) values, greatly affects the magnitude of discrepancy.

Nonetheless, inspection of Fig. 13 reveals a great deal of information. The first row of Fig. 13 and Table 2 show discrepancies between the outcomes from the emulated “typical” procedure in the literature and full PPAP. By comparing the absolute value of the median and the standard deviation of the spread, we can say that n_e is significantly underestimated, and $c(\text{H}\beta)$ to a lesser extent. Plus, the abundance maps derived from different lines differ by 10 %, roughly speaking.

The major issue of this “typical” procedure boils down to the forced uniform n_e and T_e assumption. The discrepancy between the imposed n_e and T_e and actual n_e and T_e culminates as offsets in $c(\text{H}\beta)$. For the present case, given the spread in the derived ($n_e([\text{S II}]), T_e([\text{N II}])$) values (Fig. 5), the forced uncertainties already amount roughly to 10–20 %. As the adopted n_e diagnostic curve is very much steeper than the T_e coun-

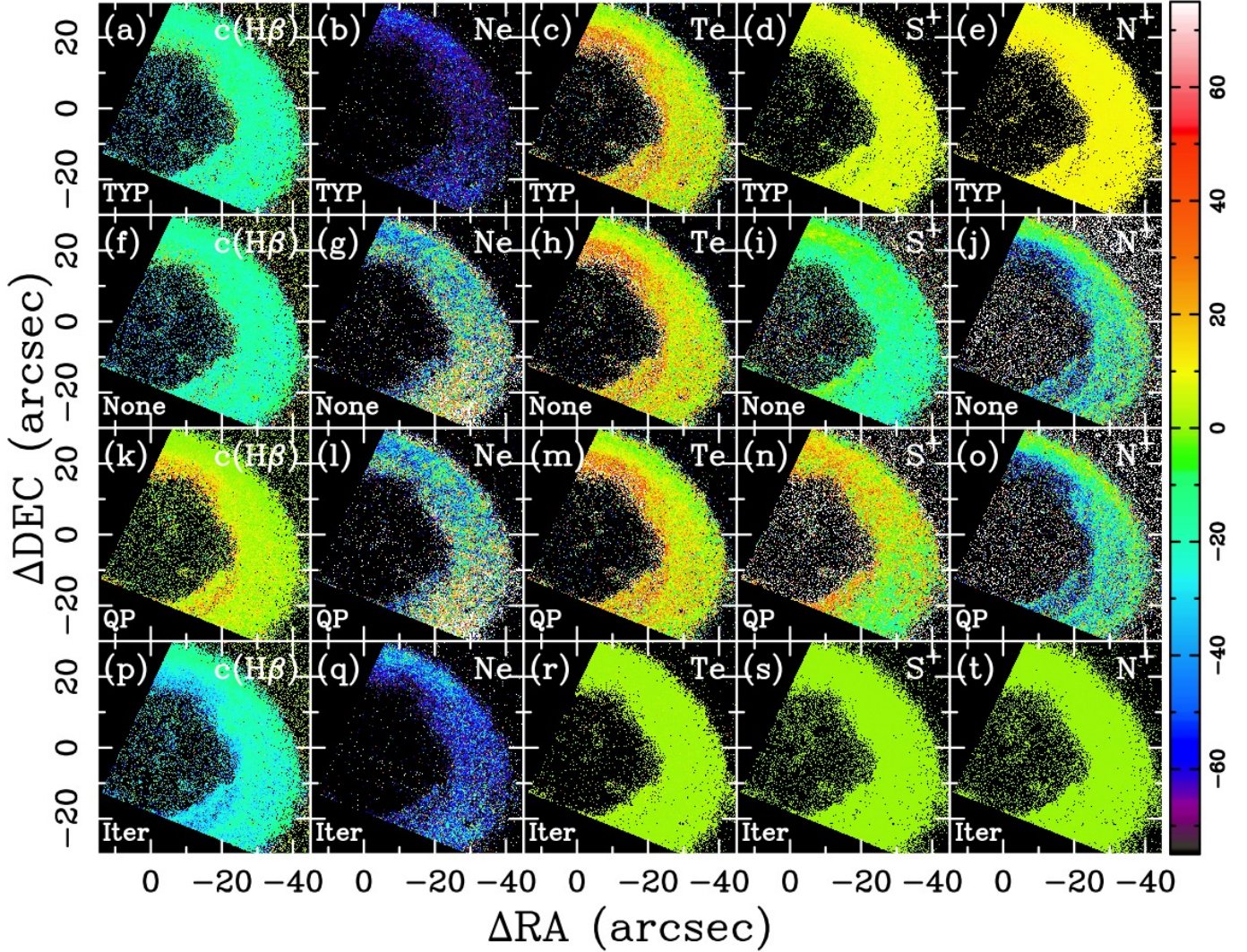


Figure 13. Graphical summary of discrepancies that result from various inconsistencies injected over the course of PPAP. The observed discrepancies are displayed in terms of the relative percentage difference distribution in $c(\text{H}\beta)$ (left-most column), n_e (second column from left), and T_e (middle column) compared to the full PPAP results (§3.1, Fig. 2; §3.2, Fig. 5) and in $n(\text{S}^+)/n(\text{H}^+)$ (second column from right), and $n(\text{N}^+)/n(\text{H}^+)$ (right-most column) between the individual results from each of the two diagnostic lines (§3.5, Fig. 11). The four different permutations of the source of inconsistencies are (1) an emulated “typical” simplified method in the literature (top row; panels a–e, marked as TYP), (2) omitting both the QP line extraction and iterative search for convergence (second row; panels f–j, marked as None), (3) executing only the QP line extraction (third row; panels k–o marked as QP), and (4) executing only the iterative search for convergence (fourth row; panels p–t marked as Iter). The color wedge on the right indicates the displayed range of the relative percentage difference between -75% to 75% . The median and standard deviation of the relative percentage difference for each case are also summarized in Table 2. Other image conventions follow those of Fig. 2.

terpart, even slight offsets in $c(\text{H}\beta)$ (and hence, in diagnostic line ratios) would influence n_e more than T_e . The greatest discrepancies of all at 65% in n_e in this procedure reminds us of its shoddiness. T_e is off by 7% on average, but we can still consider that T_e meanders around the true value. Similarly, this method is the only one among all that produces abundance maps that are not consistent with each other. Thus, this exercise exem-

plifies the inappropriateness of such a “typical” method of plasma diagnostics.

The other rows of Fig. 13 compare discrepancies among different permutations of PPAP. The difference between “TYP” and “None” is that in “None” we rigorously consider the n_e and T_e dual dependence on both of the n_e and T_e diagnostic functions. With “QP”, the mutual contamination between $\text{H}\alpha$ and $[\text{N II}]$ is addressed, and hence, the resulting $c(\text{H}\beta)$ is among the

PPAP Permutation	$\Delta c(\text{H}\beta)$ (%)	Δn_e (%)	ΔT_e (%)	$\Delta(n(\text{S}^+)/n(\text{H}^+))$ (%)	$\Delta(n(\text{N}^+)/n(\text{H}^+))$ (%)
TYP	-14 ± 11	-65 ± 17	7 ± 17	6 ± 1	8 ± 1
None	-14 ± 11	-22 ± 42	7 ± 17	-12 ± 13	-19 ± 34
QP	1 ± 4	-33 ± 42	7 ± 17	6 ± 21	-19 ± 33
Iter	-18 ± 12	-53 ± 22	$4 \pm 5 (\times 10^{-1})$	$6 \pm 343 (\times 10^{-4})$	$6 \pm 522 (\times 10^{-4})$

Table 2. Quantitative summary of discrepancies that result from various inconsistencies injected over the course of PPAP in terms of the median and standard deviation of the relative percentage difference distribution for each case shown in Fig. 13.

best (Fig. 13f,k,p). This indeed proves the significance of the QP process where appropriate. n_e turns out to be a difficult quantity to determine. But, it may be expected from the fact that the n_e diagnostic curve is a rather steep function of the adopted diagnostic line ratio. With “Iter”, what is striking is the goodness of the match we see in T_e and N^+ and S^+ abundances: the iterative process alone recovers the correct solutions for these quantities. Nevertheless, it alone cannot resolve everything. It appears that the correctness of $c(\text{H}\beta)$ and $n_e([\text{S II}])$ is sacrificed at the expense of the other quantities during the iterative optimization of the solution.

All in all, lessons learned from this exercise are very straightforward. The widely practiced simplifications of uniform n_e and T_e assumption in “typical” plasma diagnostics without considering the extinction correction simultaneously would only feed discrepancies. Both the extinction correction and plasma diagnostics must be performed altogether as an integrated process.

As for PPAP, it is *necessary* to perform the QP process (or anything takes care of spatially resolved line calibration) iterative search for converged solutions. If not, imposed inconsistencies would amplify as relative discrepancies at tens of % over the course of the whole analyses in one way or another, affecting various results seemingly at random. In other words, if self-consistency is maintained without imposing obviously unrealistic uniform n_e and T_e assumptions in performing plasma diagnostics including the extinction correction, it is possible to obtain rather exact solution for $c(\text{H}\beta)$ and (n_e, T_e) as well as other derivatives such as abundances and carry out any subsequent quantitative analyses quite rigorously.

In extreme cases where the goal is determining just T_e , however, it *may be* tolerable as long as extinction correction and plasma diagnostics are performed iteratively for converged solutions. This is possible when the T_e diagnostic curve happens to be only a weak function of the diagnostic line ratios. In that case, it is critical to remember that $c(\text{H}\beta)$ and n_e are compromised (i.e., the remaining discrepancies are absorbed as offsets in $c(\text{H}\beta)$ and n_e).

3.7. Other Caveats

3.7.1. Plasma Diagnostics with $[\text{O III}]$ Lines

For the present analyses, we adopt $[\text{S II}]$ and $[\text{N II}]$ line ratios as our primary diagnostics. Naturally, these diagnostics are suited to probe low-excitation regions in the outer part of the main ring where these emission lines are strong (Fig. 8d–h). The present data set also includes the $[\text{O III}]$ line maps at 4363 and 5007 Å (Fig. 8a,c), which provide another diagnostic line ratio for higher-excitation regions in the inner part of the main ring. The difference in the spatial coverage among these diagnostics is evident from the line ratio maps (Fig. 10). This spatial anti-correlation is actually a critical point to consider in plasma diagnostics, especially when selecting two diagnostics as a pair. However, this view was often neglected in the past because spectra were rarely taken in a spatially resolved manner. Therefore, it is instructive to closely examine how plasma diagnostics work out taking into account the spatial distribution of diagnostic lines, especially when one deals with spatially resolved spectral images.

Fig. 14 presents the n_e - T_e diagram at four positions in the main ring. Panels (a) and (b) are of a local peak in $[\text{O III}]$ (Fig. 8e,g) near the inner and outer edge of the main ring along the short axis (i.e. NNW direction). Similarly, panels (c) and (d) are of a local peak in $[\text{N II}]$ (Fig. 8d–f) and $[\text{S II}]$ (Fig. 8g,h) as well as $[\text{O III}]$ near the inner and outer edge of the main ring along the long axis (i.e. NSW direction), respectively. These n_e - T_e diagrams evidently show how each of the $[\text{S II}]$, $[\text{N II}]$, and $[\text{O III}]$ diagnostic line ratios behaves differently at each position because of the local physical conditions (Fig. 14).

As reviewed in § 2.3.2, any given diagnostic line ratio can be expressed as a non-linear function of n_e and T_e . Hence, each line ratio takes the form of a curve in the n_e - T_e space as shown in Fig. 14. The shaded thickness for each line represents uncertainties propagated from the assumed 20 % uncertainty in the extinction correction. Then, the intersection of two diagnostic curves would specify n_e and T_e , provided that the corresponding emission lines arise from the same region of the target nebula. Because these curves are non-linear functions, intersections can only be determined numerically. This is indeed why plasma diagnostics must be done as an iterative process.

In addition, for such a numerical n_e and T_e search to proceed optimally, an n_e diagnostic should cover a wide range of T_e at nearly constant n_e . Similarly, a T_e diag-

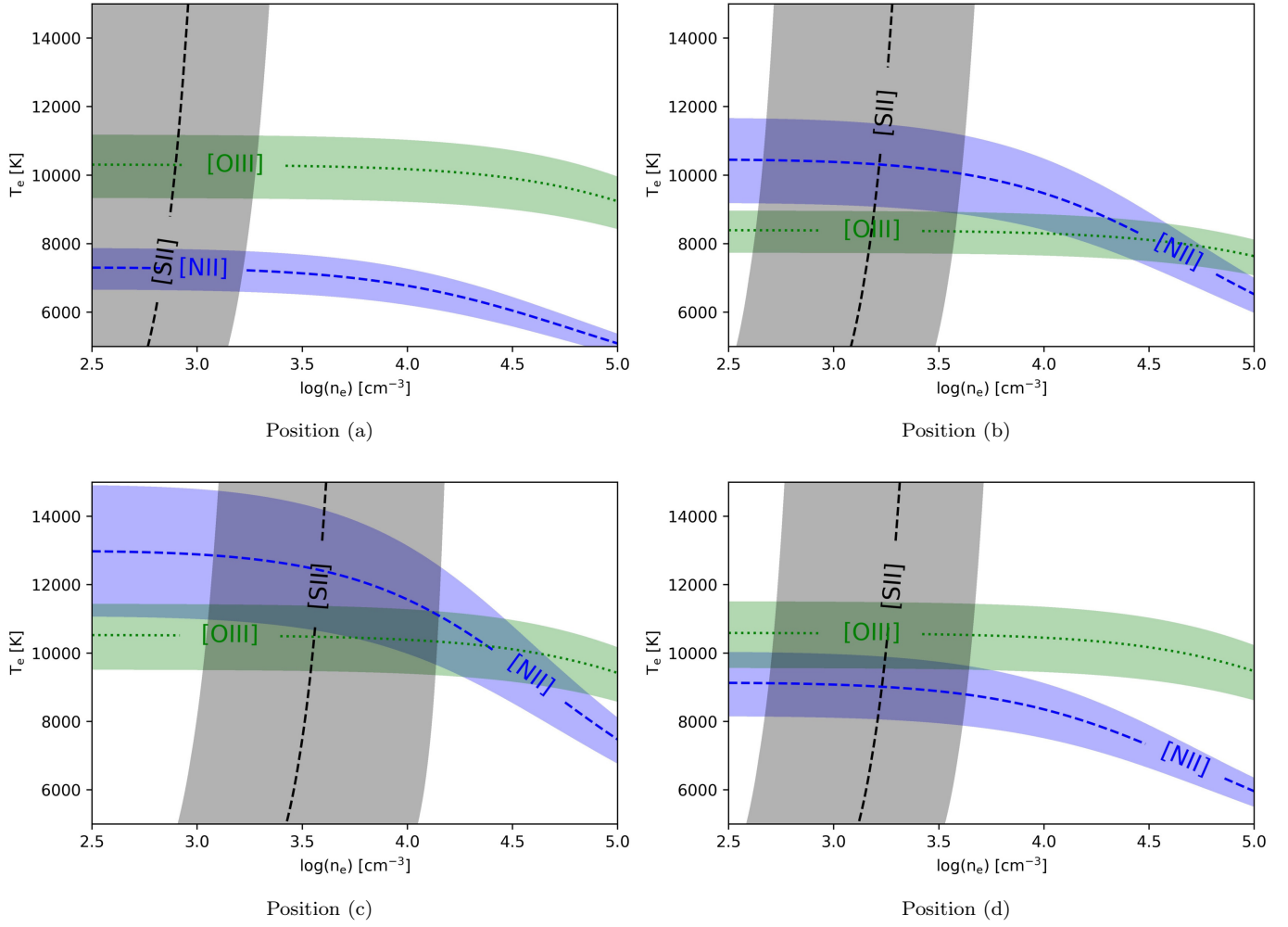


Figure 14. The n_e - T_e diagrams for the range of $10^{2.5} < n_e < 10^5 \text{ cm}^{-3}$ and $5,000 < T_e < 15,000 \text{ K}$, showing the [S II], [N II], and [O III] diagnostic curves at four local emission peaks in NGC 6720: (a) the inner edge of the main ring along the short axis, (b) the outer edge of the main ring along the short axis, (c) the inner edge of the main ring along the long axis, and (d) the outer edge of the main ring along the long axis. The thickness of each diagnostic curve represents uncertainties propagated from the assumed 20% uncertainty in the input line ratio.

nostic should cover a wide range of n_e at nearly constant T_e . This is because we would like an n_e diagnostic immune to the *wrong* initial T_e guesstimate so that the inherent T_e dependence of the diagnostic can be ignored, and vice versa. Still, for the optimal results, both n_e and T_e should be simultaneously determined by seeking convergence through a nested iterative process.

As demonstrated by Fig. 14, diagnostic curves intersect with each other at multiple positions in the n_e - T_e space. This exemplifies the fact that we cannot indiscriminately choose any pair of diagnostic lines, especially because differences of a few hundred cm^{-3} and a few thousand K can easily cause at least tens of % difference in the resulting abundances as shown above at the end of § 3.5. Ideally, we should like to select n_e and T_e diagnostics that are of similar transition energies arising from the same part of the target object. If not, the re-

sulting n_e and T_e can easily be off by a few thousands K and/or a couple of hundreds of cm^{-3} , and hence, several tens of % discrepancies in the resulting abundances.

3.7.2. Contamination by He II Lines

As shown in Fig. 8b, the He II 4686 Å line is reasonably strong: its relative strength to H β is as strong as the [S II] 6717/31 Å doublet and roughly $\sim 10\%$ of H α . Thus, the effect of the He II line contamination in the H α and H β maps needs to be assessed. If it is significant, the resulting $c(\text{H}\beta)$, and subsequently, $n_e([\text{S II}])$, and $T_e([\text{N II}])$, will be compromised, and will have to be corrected for accordingly. To this end, we perform the iterative derivation of $c(\text{H}\beta)$, $n_e([\text{S II}])$, and $T_e([\text{N II}])$ one more time using the H α and H β maps from which their respective contaminating He II lines at 6560 and 4859 Å removed.

This consideration actually adds another layer of complication in PPAP, because now we have to know the extinction, $c(\lambda)$, in order to derive the very extinction itself at Step (2). More specifically, the observed $H\alpha$ -to- $H\beta$ ratio that is needed to derive $c(H\beta)$ (Eq. (2)) has to be replaced by the version of the $H\alpha$ -to- $H\beta$ ratio from which He II contamination is subtracted. However, to calculate the He II line flux distribution at 6560 and 4859 Å (the contaminants to be subtracted from the $H\alpha$ and $H\beta$ maps, respectively), the *extinction-corrected* He II 4686 Å map needs to be scaled by an appropriate theoretical line ratio (e.g. Hummer & Storey 1987; Hummer & Storey 1998; Storey & Hummer 1995), i.e.

$$\begin{aligned} & \frac{I(H\alpha) - I(\text{He II})_{6560}}{I(H\beta) - I(\text{He II})_{4859}} \\ &= \frac{I(H\alpha) - I_0(\text{He II})_{6560} \cdot 10^{-c(6560)}}{I(H\beta) - I_0(\text{He II})_{4859} \cdot 10^{-c(4859)}} \\ &= \frac{I(H\alpha) - I_0(\text{He II})_{4686} \cdot R\left(\frac{6560}{4686}\right) \cdot 10^{-c(6560)}}{I(H\beta) - I_0(\text{He II})_{4686} \cdot R\left(\frac{4859}{4686}\right) \cdot 10^{-c(4859)}}, \\ &= \frac{I(H\alpha) - I(\text{He II})_{4686} \cdot 10^{c(4686)} \cdot R\left(\frac{6560}{4686}\right) \cdot 10^{-c(6560)}}{I(H\beta) - I(\text{He II})_{4686} \cdot 10^{c(4686)} \cdot R\left(\frac{4859}{4686}\right) \cdot 10^{-c(4859)}}, \\ &= \frac{I(H\alpha) - I(\text{He II})_{4686} \cdot R\left(\frac{6560}{4686}\right) \cdot 10^{c(4686)-c(6560)}}{I(H\beta) - I(\text{He II})_{4686} \cdot R\left(\frac{4859}{4686}\right) \cdot 10^{c(4686)-c(4859)}}, \end{aligned}$$

where $R(\lambda_1/\lambda_2)$ is the theoretical He II line ratio between wavelengths at λ_1 and λ_2 (which is a function of $n_e([\text{S II}])$ and $T_e([\text{N II}])$; e.g. Hummer & Storey 1987; Hummer & Storey 1998; Storey & Hummer 1995) and the subscripted values refer to the line wavelengths.

Using this $H\alpha$ -to- $H\beta$ ratio without the He II contamination, we perform the same iterative processing to obtain the $c(H\beta)$, $n_e([\text{S II}])$, and $T_e([\text{N II}])$ maps. This modification tends to increase the $H\alpha$ -to- $H\beta$ ratio slightly, and hence, tends to increase the resulting $c(H\beta)$ slightly. The difference of the $c(H\beta)$ values before and after applying this He II contamination removal is quantified as the percentage difference ratio, $(c(H\beta) - c(H\beta)_{\text{no He II}})/c(H\beta)_{\text{no He II}}$, and plotted as a radial profile in Fig. 15.

The revised $c(H\beta)$ with the He II contamination mitigated comes out slightly greater. Thus, the He II contamination turns out greater in $H\beta$ than in $H\alpha$ in the present case. As a result, the percentage difference ratio comes out to be negative. The difference is minor in the outer part of the main ring ($> 25''$; at $-2.9 \pm 12.7\%$), and hence, the revised $n_e([\text{S II}])$ and $T_e([\text{N II}])$ distributions do not show much difference. On the other hand, the difference increases progressively toward the inner edge of the main ring ($< 25''$): the difference becomes as large as $\sim 20\%$ at the inner edge ($\sim 20''$).

It appears that the relative amount of the He II contamination grows greater toward the center of the main ring into the inner cavity. This agrees with the expectation that the effects of the He II contamination is greater

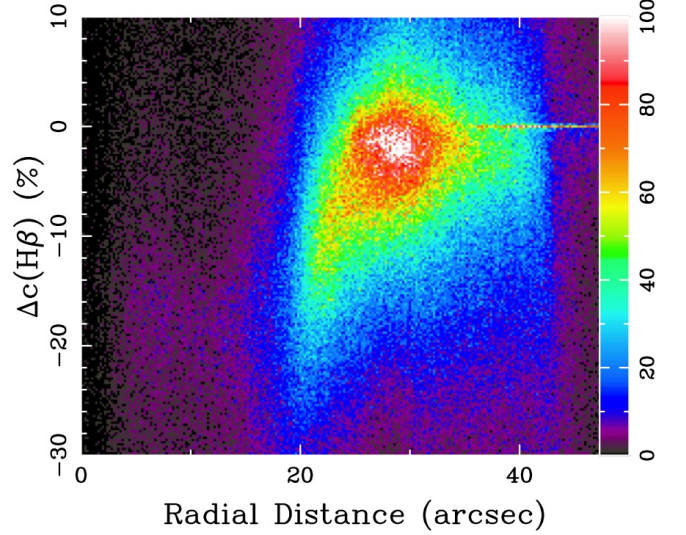


Figure 15. The radial density distribution of the percentage difference in $c(H\beta)$ compared to the results without the He II contamination. The original $c(H\beta)$ result (with the He II contamination) is underestimated especially in the inner half of the main ring interfacing with the high-excitation central cavity ($< 25''$). The 0% region seen beyond $35''$ is the no-data part beyond the outer edge of the main ring.

where the degree of excitation is higher. For the present case of NGC 6720, it appears that only the inner cavity is where the He II contamination needs to be seriously mitigated, as also suggested from its spatial distribution (Fig. 8b). Thus, we conclude that the He II contamination must be properly assessed when determining quantities pertaining to high-excitation ionic species (such as He II, of course).

3.7.3. Contribution by Recombination

We should also bear in mind that strong recombination lines may influence the T_e determination (e.g. Liu et al. 2000; Gómez-Llanos et al. 2020). For the present case, the $[\text{N II}] 5755 \text{ \AA}$ line flux may be enhanced by recombination from the N^{2+} lines to the said line, and that the resulting $T_e([\text{N II}])$ may not solely be of collision.

This is, however, not likely for NGC 6720. Zhang et al. (2004) reported that such contribution by recombination was extremely small in this nebula. Also, based on the far-IR line emission maps obtained with the *Herschel Space Observatory* as part of the *Herschel Planetary Nebula Survey* (Ueta et al. 2014), we can see that the spatial distributions of the $[\text{N II}] 122 \mu\text{m}$ and $[\text{N III}] 57 \mu\text{m}$ lines (not shown here; Ueta et al. *in preparation*) show similar spatial differences as we see between the $[\text{N II}] 5755/6548/6583 \text{ \AA}$ lines and the $[\text{O III}] 4363/5007 \text{ \AA}$ lines (Fig. 8).

When such contribution by recombination is expected to be significant, one needs to assess and remove the N^{2+} contribution by recombination. Under PPAP, we can do

so by adding another iterative loop, as done to mitigate contamination by He II lines (see § 3.7.2). For example, using $T_e([\text{O III}])$, $n_e([\text{Cl III}])$, and $[\text{N III}]$ collisional excitation line maps (e.g. at 1750 \AA or $57 \mu\text{m}$), one can synthesise the map from N^{2+} recombination contribution to $[\text{N II}] 5755 \text{ \AA}$ by following Eq.(1) of Liu et al. (2000). Subsequently, the updated $[\text{N II}] 5755 \text{ \AA}$ line flux, which represents purely collisionally excited line flux, is used to compute $T_e([\text{N II}])$ and $n_e([\text{S II}])$ and derive $c(\text{H}\beta)$, which would then update the extinction corrected line maps for the next round of the iteration.

4. SUMMARY

We have established a proper plasma analysis practice (PPAP), a streamlined iterative procedure that integrates the extinction correction and plasma diagnostics for spatially extended targets in one go (§ 2.3; Fig. 1). The major strength of PPAP is that it requires nothing other than just the input spectral images of critical diagnostic lines plus the choice of the extinction law and R_V value to adopt. In other words, there is absolutely no need to assume anything.

This work is motivated by the recognized but subtle dependence of the power-law extinction index, $c(\lambda)$, on both the electron density and temperature, (n_e , T_e), which are the very quantities that must be known to determine $c(\lambda)$. Such circular dependence must be resolved via an iterative process looking for the optimum $c(\text{H}\beta)$ (which is $c(\lambda)$ at $\text{H}\beta$) and (n_e , T_e) values for convergence. Unfortunately, however, these interdependent analyses have rarely been considered altogether as one in the past.

With this in mind, using a suite of narrowband filter images of NGC 6720 taken with WFC3 on *HST*, we have derived by following PPAP a self-consistent and spatially-resolved solution of $c(\text{H}\beta)$ (§ 3.1; Fig. 2) and (n_e , T_e) (§ 3.2; Fig. 5) for the object simultaneously. In the present exercise, the obtained solution pertains to the NW quadrant of the main ring structure in NGC 6720, for which critical diagnostic line maps are available (e.g. the low-excitation $[\text{S II}]$ and $[\text{N II}]$ diagnostic line ratio maps).

The derived $c(\text{H}\beta)$ and ($n_e([\text{S II}])$, $T_e([\text{N II}])$) maps clearly reveal spatial variations within the nebula, which would not have been uncovered if uniform (n_e , T_e) were assumed, in unprecedented detail. Also, the $c(\text{H}\beta)$ map correctly accounts for both the ISM and circumsource components (Fig. 3) to the whole extent of the nebula for which we have measurements. The ionized gas-to-dust mass ratio in the main ring is found to be fairly spatially varying with the median of 437 ± 357 , much greater than the canonical value of 100 (§ 3.3; Fig. 7). The total gas-to-dust mass ratio in the main ring of NGC 6720 is estimated to be about 1600. Moreover, we have obtained properly extinction-corrected line emission maps (§ 3.4; Fig. 8) as well as the relative ionic abundance distribu-

tion maps (N^+ and S^+ relative to H^+ ; § 3.5; Fig. 11) as the essential products of plasma diagnostics.

We have demonstrated that difference of only a few hundred cm^{-3} in n_e or a few thousand K in T_e (commonly seen as the amount of spatial variations; Fig. 6) can introduce differences in tens of % in the resulting metal abundances (Fig. 12). Therefore, in the era of spatially-resolved spectroscopy, we cannot afford to continue this old tradition of assuming constant n_e and T_e (among other things) without paying attention to the interdependence between extinction correction and plasma diagnostics as well as self-consistency among parameters. If we perform plasma diagnostics without PPAP, we will not be able to maintain the integrity of data at each spatial element. This is because results of such analyses will always suffer from uncertainties at tens of % that can easily arise from inconsistencies introduced by the unnecessary assumptions. This will simply defeats the purpose of conducting spatially-resolved spectroscopy in the first place.

We have also evaluated how much discrepancies can arise at each step of the process if PPAP is not strictly followed (§ 3.6; Fig. 13; Table 2). Our analyses have demonstrated that plasma diagnostics typically practiced in the literature and/or neglecting PPAP even partially would sustain uncertainties greater than 10 %. We have also estimated that for PPAP to be effective n_e and T_e diagnostic line fluxes need to be determined at uncertainties better than 10 % in general.

The strength of securing self-consistent n_e and T_e (and $c(\text{H}\beta)$) has been vindicated by the fact that multiple $n(\text{N}^+)/n(\text{H}^+)$ and $n(\text{S}^+)/n(\text{H}^+)$ distribution maps derived from the corresponding $[\text{N II}]$ and $[\text{S II}]$ line maps of distinct transitions come out to be identical. Such a feat has never been accomplished in plasma diagnostics with spectral imaging data in the past. Only by adopting PPAP fully and not incorporating any assumptions that would degrade the observational data in any way (especially spatially), we can obtain robust outcomes.

Furthermore, there are always certain sets of diagnostic lines that are suited to probe particular parts of target sources, like the $[\text{N II}]$ and $[\text{S II}]$ line ratio pair that probes low-excitation regions. One should always be conscious about which n_e and T_e diagnostic lines to use depending on different local physical conditions to be probed (§ 3.7.1). To that end, when probing high-excitation regions for which the $[\text{O III}]$ lines or other diagnostic lines of the same and higher transition energy regimes work, one should like to remove contamination in H lines by He II lines and consider contribution by strong recombination lines in metal lines for optimum results (§ 3.7.2).

Various lessons learned from the present exercise are;

1. Plasma diagnostics should really be performed with the extinction correction as an integrated iterative procedure for the best results.

2. We should remind ourselves that the theoretical $H\alpha$ -to- $H\beta$ ratio (or any H I line ratio) is a function of n_e and T_e and never a constant.
3. Imposing (n_e, T_e) constancy in plasma diagnostics will inject uncertainties at tens of % in the outcomes of the analyses. In the literature, such uncertainties are often attributed to the local fluctuations of physical conditions. In reality, the initial constancy assumption is what amplifies uncertainties: PPAP can resolve such local fluctuations.

4. As long as self-attenuation by the circumsource material is expected, it is wrong to adopt the ISM extinction value for target sources, as the non-negligible circumsource extinction will be surely missed (and make (n_e, T_e) incorrect).
5. By the same token, it is incorrect to indiscriminately adopt the empirical $A(V)$ -to- N_H relation for ISM when some non-negligible amount of circumsource attenuation is expected, as the ISM relation implicitly assumes the gas-to-dust mass ratio of 100, which is not necessarily true for individual target sources.

APPENDIX

A. QP LINE EXTRACTION

Using the adopted WFC3 images with the QP method (Ueta et al. 2019), we can separate (i) the $H\alpha$ map at 6563 Å and the [N II] maps at 6548 and 6583 Å from the F656N and F658N image pair, (ii) the [S II] maps at 6717 and 6731 Å from any pair among the FQ672N, F673N, and FQ674N images, and (iii) the $H\gamma$ map at 4340 Å and the [O III] map at 4363 Å from the FQ436N and FQ437N image pair. The nebular continuum is determined by taking the mean of the three “continuum” band images (F547M, F645N, and FQ750N) as long as pixel values register with $S/N \geq 3$.

Here, the continuum emission is assumed to be distributed more or less similarly across the relevant spectral range. Then, to subtract the continuum from each emission band map, an appropriate scaling factor of the averaged continuum map is determined using the integrated ADU counts³ of about 10 field stars that appear in the FoV of both the continuum and emission band images. For this work, we implement the QP algorithm anew in Python by adopting the Operator Splitting Quadratic Program (OSQP) solver (Stellato et al. 2020).⁴

A.1. $H\alpha$ and [N II]

For the $H\alpha$ and [N II] line separation, we employ the following two conditions, (i) the positivity condition (i.e. derived line fluxes cannot be negative) and (ii) the theoretical line strength ratio of the [N II] 6583 Å line to the [N II] 6548 Å line being 2.96 (Ueta et al. 2019). The second condition is relevant only in separating $H\alpha$ and [N II] lines from the F656N and F658N pair: we use only the positivity condition in separating other lines.

³ The native counts of the archived *HST* data, usually referred to as the Data Numbers (DNs), in e^- or e^-s^{-1} , depending on the instrument (Desjardins & Lucas 2019).

⁴ Available from <https://github.com/oxfordcontrol/osqp>

As required by the QP formulation, all the input images are taken to have been modulated by the system throughput. Thus, we multiply the input WFC3 images from the archive by the bandpass unit response (which is the value stored under the PHOTFLAM keyword in the FITS image header and converts the original pixel count into the flux density at $\text{erg s}^{-1} \text{cm}^{-2} \text{Å}^{-1}$) and the bandpass equivalent width (which modulates the surface brightness of the bandpass by the corresponding system throughput) computed via PYSYNPHOT (Lim et al. 2015). The QP process then extracts line flux distribution maps of $H\alpha$ 6563 Å, [N II] 6548 Å, [N II] 6583 Å, [S II] 6717 Å, [S II] 6731 Å, $H\gamma$ at 4340 Å, and [O III] 4363 Å in $\text{erg s}^{-1} \text{cm}^{-2} \text{pix}^{-1}$ as observed (i.e.

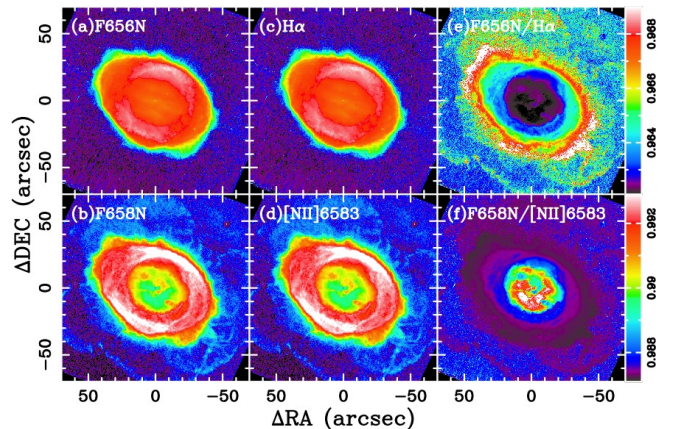


Figure 16. Summary of the QP extraction of the $H\alpha$ and [N II] 6583 Å line maps from the F656N and F658N images. From top-left to bottom-right, (a) F656N, (b) F658N, (c) QP-extracted $H\alpha$, and (d) QP-extracted [N II] 6583 Å line flux maps (in $\text{erg s}^{-1} \text{cm}^{-2} \text{pix}^{-1}$; log-scaled from $10^{-15.5}$ to $10^{-18.5}$) and (e) F656N-to- $H\alpha$ and (f) F658N-to-[N II] 6583 Å line flux ratio maps (the wedge on the right indicating the range of the displayed ratio). Image conventions follow those for the $c(H\beta)$ map in Fig. 2.

modulation by the system throughput is corrected for, but the extinction is not yet corrected for). Other narrowband images that can isolate each of the corresponding target lines are multiplied by the bandpass unit response and the bandpass rectangular width (which is the equivalent width divided by the maximum system throughput in the bandpass) to convert the pixel units to flux ($\text{ergs}^{-1} \text{cm}^{-2} \text{pix}^{-1}$; modulation by the system throughput is corrected for, but the extinction is not yet corrected for) for subsequent processes with the QP-extracted line maps.

Fig. 16 shows the original WFC3 filter images of F656N (panel a) and F658N (panel b) and the QP-extracted $\text{H}\alpha$ (panel c) and $[\text{N II}] 6583 \text{ \AA}$ (panel d) line flux maps, along with the original-to-QP line flux ratio maps (panels e and f) of NGC 6720. These results are consistent with the previous results (Ueta et al. 2019), straightforwardly demonstrating the power of the QP line extraction. For the present work, we display the surface brightness distribution in the “petal” structures beyond the main ring, in which the S/N ratio to show that the faint petal emission is largely of low-excitation $[\text{N II}]$ (Lame & Pogge 1994; Martin et al. 2016).

The F656N-to- $\text{H}\alpha$ flux ratio tends to be low in the central cavity of the main ring (up to $\sim 5\%$; Fig. 16e). The F658N-to- $[\text{N II}] 6583 \text{ \AA}$ flux ratio map shows lower ratios near the periphery of the main ring (a few %; Fig. 16f). This means that if the F656N map is blindly adopted to represent the $\text{H}\alpha$ emission distribution, the $\text{H}\alpha$ emission would be underestimated by at least 3% in the periphery of the main ring and up to $\sim 5\%$ in the central cavity. Similarly, if the F658N map is hastily taken to represent the $[\text{N II}] 6583 \text{ \AA}$ emission distribution, the $[\text{N II}] 6583 \text{ \AA}$ emission would be underestimated by about 1% in the central cavity and up to $\sim 2\%$ in the main ring. These differences may be small, but will be compounded in the subsequent analyses to cause greater inconsistencies.

More importantly, we must remind ourselves that the spatial distribution of $\text{H}\alpha$ and $[\text{N II}]$ is different to begin with. $\text{H}\alpha$ generally represents the ionized region, whereas $[\text{N II}]$ usually corresponds to the lower-temperature PDR. Therefore, if both the $\text{H}\alpha$ and $[\text{N II}]$ line maps suffer from mutual line blending, the line ratio map between them tends to be marginalized, i.e., any structures we observe as $\text{H}\alpha$ -to- $[\text{N II}]$ ratio variations tend to be “washed out” as we see in the petal structures. For example, this $\text{H}\alpha$ -to- $[\text{N II}]$ marginalization would blur the location of the ionization front (IF) that presumably exists where the $\text{H}\alpha$ -to- $[\text{N II}]$ gradient tends to be large. Thus, keeping the spatial consistency is important in investigating spatially resolved line emission.

A.2. $[\text{S II}] 6717 \text{ and } 6731 \text{ \AA}$

Fig. 17 displays the QP results for the $[\text{S II}] 6717/31 \text{ \AA}$ line pair. For this group, QP processing can be used with any pair of the three maps or all three maps among

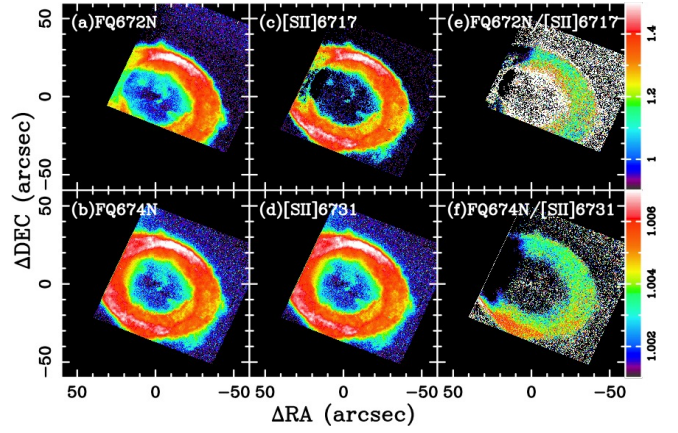


Figure 17. Same as Fig. 16, but for the $[\text{S II}] 6717$ and 6731 \AA line maps from the FQ672N and FQ674N images and log-scaled flux distribution from $10^{-16.5}$ to $10^{-18.5} \text{ ergs}^{-1} \text{ cm}^{-2} \text{ pix}^{-1}$.

the FQ672N (panel a), F673N (not shown), and FQ674N (panel b) filters. For the present analysis, we opt to use the F673N and FQ674N pair because this pair covers the largest extent of the nebula. The FQ674N filter isolates $[\text{S II}] 6731 \text{ \AA}$ (panel d) emission fairly well (less than 1% difference; panel f), while the FQ672N filter suffers from line blending as high as few 10s of % (panel e). We note that the NE and SE edges of the map are affected by the quad-filter edge effect (§ 6.5 of Dressel 2019; panel f).

As we will see below, the $[\text{S II}]$ maps at 6717 \AA (panel c) and 6731 \AA (panel d) play a critical role in determining $n_e([\text{S II}])$. Hence, the extent of $[\text{S II}]$ emission sets the maximum spatial extent where the present full 2-D plasma diagnostics would be valid. Practically, this means that results of the subsequent 2-D plasma diagnostics are valid only in the NW quadrant of the main ring (see § 3.7).

A.3. $\text{H}\gamma$ and $[\text{O III}] 4363 \text{ \AA}$

Fig. 18 presents the original WFC3 quad-filter images of FQ436N (panel a) and FQ437N (panel b) and the QP-extracted line flux maps of $\text{H}\gamma$ (panel c) and $[\text{O III}] 4363 \text{ \AA}$ (panel d), as well as the corresponding original-to-QP line flux ratio maps (panels e–f). The $\text{H}\gamma$ emission captured by the FQ436N filter is very little as the system throughput at $\text{H}\gamma$ is only 1.7%. Hence, the recovered $\text{H}\gamma$ surface brightness is fairly uncertain ($\text{S/N} < 2$ even at the brightest region). Even if a reasonably high S/N is achieved in the $\text{H}\gamma$ map, because the transition energy of $\text{H}\gamma$ is higher than $\text{H}\alpha$ and $\text{H}\beta$, the spatial extent covered by $\text{H}\gamma$ is more restricted, covering the higher-temperature regions than $\text{H}\alpha$ and $\text{H}\beta$ do. For the present work, therefore, we adopt the QP-recovered $\text{H}\alpha 6563 \text{ \AA}$ (Fig. 16e), $[\text{N II}] 6583 \text{ \AA}$ (Fig. 16f), $[\text{S II}] 6717 \text{ \AA}$ (Fig. 17e), and $[\text{S II}] 6731 \text{ \AA}$ (Fig. 17f) maps as well as the original $\text{H}\beta (= \text{F486N})$ and $[\text{N II}] 5755 \text{ \AA}$

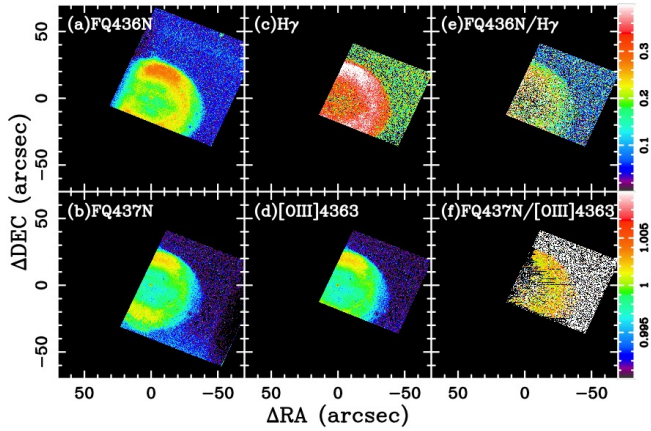


Figure 18. Same as Fig. 16, but for the $H\gamma$ and $[O\text{ III}] 4363\text{ \AA}$ line maps from the FQ436N and FQ437N images and log-scaled flux distribution from $10^{-16.5}$ to $10^{-18.5}$ $\text{erg s}^{-1} \text{cm}^{-2} \text{pix}^{-1}$.

(= FQ575N; Fig. 8h) maps because of their reasonable S/N and decent spatial coverage.

Facilities: HST(WFC3)

Software: Astropy (Astropy Collaboration et al. 2013, 2018), PyNeb (Luridiana et al. 2015), PySynphot (Lim et al. 2015), OSQP (Stellato et al. 2020)

1 Based on observations made with the NASA/ESA Hub-
 2 ble Space Telescope, and obtained from the Hubble
 3 Legacy Archive, which is a collaboration between the
 4 Space Telescope Science Institute (STScI/NASA), the
 5 Space Telescope European Coordinating Facility (ST-
 6 ECF/ESA) and the Canadian Astronomy Data Centre
 7 (CADC/NRC/CSA).

8 This research made use of Astropy, a community-
 9 developed core Python package for Astronomy (Astropy
 10 Collaboration et al. 2013, 2018) and PyNeb, a toolset
 11 dedicated to the analysis of emission lines (Luridiana
 12 et al. 2015), as well as OSQP, a convex quadratic pro-
 13 grams solver (Stellato et al. 2020).

14 TU was supported partially by the National Aero-
 15 nautics and Space Administration under Grant No.
 16 NNX15AF24G issued through the Mission Directorate
 17 and by the Japan Society for the Promotion of Sci-
 18 ence (JSPS) through its invitation fellowship program
 19 (FY2020, long-term). MO was supported by JSPS
 20 Grants-in-Aid for Scientific Research(C) (JP19K03914).

21 Authors thank Dr. Bob O’Dell for having email dis-
 22 cussions about the use of the present *HST*/WFC data
 23 set for NGC 6720 and providing valuable comments after
 24 reading an early version of the manuscript.

REFERENCES

- Astropy Collaboration, Robitaille, T. P., Tollerud, E. J.,
 et al. 2013, *A&A*, 558, A33,
 doi: [10.1051/0004-6361/201322068](https://doi.org/10.1051/0004-6361/201322068)
- Astropy Collaboration, Price-Whelan, A. M., Sipőcz, B. M.,
 et al. 2018, *AJ*, 156, 123, doi: [10.3847/1538-3881/aabc4f](https://doi.org/10.3847/1538-3881/aabc4f)
- Barker, T. 1980, *The Astrophysical Journal*, 240, 99,
 doi: [10.1086/158210](https://doi.org/10.1086/158210)
- Barker, T. 1987, *ApJ*, 322, 922, doi: [10.1086/165787](https://doi.org/10.1086/165787)
- Cardelli, J. A., Clayton, G. C., & Mathis, J. S. 1989, *ApJ*,
 345, 245, doi: [10.1086/167900](https://doi.org/10.1086/167900)

- Desjardins, T., & Lucas, R. 2019, Introduction to the Hubble Space Telescope Data Handbooks, Version 9.0 (Baltimore, MD: STScI)
- Draine, B. T. 2003, *ARA&A*, 41, 241, doi: [10.1146/annurev.astro.41.011802.094840](https://doi.org/10.1146/annurev.astro.41.011802.094840)
- Dressel, L. 2019, Wide Field Camera 3 Instrument Handbook, Version 12.0 (Baltimore, MD: STScI)
- Drissen, L., Martin, T., Rousseau-Nepton, L., et al. 2019, *Monthly Notices of the Royal Astronomical Society*, 485, 3930, doi: [10.1093/mnras/stz627](https://doi.org/10.1093/mnras/stz627)
- Fischer, C. F., & Tachiev, G. 2004, *Atomic Data and Nuclear Data Tables*, 87, 1, doi: <https://doi.org/10.1016/j.adt.2004.02.001>
- Garnett, D. R., & Dinerstein, H. L. 2001, *The Astrophysical Journal*, 558, 145, doi: [10.1086/322452](https://doi.org/10.1086/322452)
- Gómez-Llanos, V., Morisset, C., García-Rojas, J., et al. 2020, *MNRAS*, 498, L82, doi: [10.1093/mnrasl/slaa131](https://doi.org/10.1093/mnrasl/slaa131)
- Gontcharov, G. A. 2012, *Ast. Lett.*, 38, 87, doi: [10.1134/S1063773712010033](https://doi.org/10.1134/S1063773712010033)
- Gontcharov, G. A., & Mosenkov, A. V. 2017, *MNRAS*, 472, 3805, doi: [10.1093/mnras/stx2219](https://doi.org/10.1093/mnras/stx2219)
- Guerrero, M. A., Manchado, A., & Chu, Y. 1997, *The Astrophysical Journal*, 487, 328, doi: [10.1086/304582](https://doi.org/10.1086/304582)
- Hawley, S. A., & Miller, J. S. 1977, *The Astrophysical Journal*, 212, 94, doi: [10.1086/155023](https://doi.org/10.1086/155023)
- Hester, J. J. 2008, *ARA&A*, 46, 127, doi: [10.1146/annurev.astro.45.051806.110608](https://doi.org/10.1146/annurev.astro.45.051806.110608)
- Hummer, D. G., & Storey, P. J. 1987, *Monthly Notices of the Royal Astronomical Society*, 224, 801, doi: [10.1093/mnras/224.3.801](https://doi.org/10.1093/mnras/224.3.801)
- Hummer, D. G., & Storey, P. J. 1998, *MNRAS*, 297, 1073, doi: [10.1046/j.1365-8711.1998.2970041073.x](https://doi.org/10.1046/j.1365-8711.1998.2970041073.x)
- Kewley, L. J., Nicholls, D. C., & Sutherland, R. S. 2019, *Annual Review of Astronomy and Astrophysics*, 57, 511, doi: [10.1146/annurev-astro-081817-051832](https://doi.org/10.1146/annurev-astro-081817-051832)
- Kwok, S. 2000, *Cambridge Astrophysics Series*, 33
- Lame, N. J., & Pogge, R. W. 1994, *AJ*, 108, 1860, doi: [10.1086/117199](https://doi.org/10.1086/117199)
- Lim, P. L., Diaz, R. I., & Laidler, V. 2015, *PySynphot User's Guide* (Baltimore, MD: STScI). <https://pysynphot.readthedocs.io/en/latest/>
- Liu, X. W., Storey, P. J., Barlow, M. J., et al. 2000, *MNRAS*, 312, 585, doi: [10.1046/j.1365-8711.2000.03167.x](https://doi.org/10.1046/j.1365-8711.2000.03167.x)
- Liu, Y., Liu, X. W., Barlow, M. J., & Luo, S. G. 2004, *MNRAS*, 353, 1251, doi: [10.1111/j.1365-2966.2004.08156.x](https://doi.org/10.1111/j.1365-2966.2004.08156.x)
- Luridiana, V., Morisset, C., & Shaw, R. A. 2015, *A&A*, 573, A42, doi: [10.1051/0004-6361/201323152](https://doi.org/10.1051/0004-6361/201323152)
- Martin, T. B., Prunet, S., & Drissen, L. 2016, *Monthly Notices of the Royal Astronomical Society*, 463, 4223, doi: [10.1093/mnras/stw2315](https://doi.org/10.1093/mnras/stw2315)
- Nicholls, D. C., Kewley, L. J., & Sutherland, R. S. 2020, *Publications of the Astronomical Society of the Pacific*, 132, 033001, doi: [10.1088/1538-3873/ab6818](https://doi.org/10.1088/1538-3873/ab6818)
- O'Dell, C. R., Ferland, G. J., Henney, W. J., & Peimbert, M. 2013a, *AJ*, 145, 92, doi: [10.1088/0004-6256/145/4/92](https://doi.org/10.1088/0004-6256/145/4/92)
- . 2013b, *AJ*, 145, 93, doi: [10.1088/0004-6256/145/4/93](https://doi.org/10.1088/0004-6256/145/4/93)
- . 2013c, *AJ*, 145, 170, doi: [10.1088/0004-6256/145/6/170](https://doi.org/10.1088/0004-6256/145/6/170)
- . 2021, *AJ*, submitted
- O'Dell, C. R., & Handron, K. D. 1996, *AJ*, 111, 1630, doi: [10.1086/117902](https://doi.org/10.1086/117902)
- O'Dell, C. R., Sabbadin, F., & Henney, W. J. 2007, *The Astronomical Journal*, 134, 1679
- Osterbrock, D. E., & Ferland, G. J. 2006, *Astrophysics of gaseous nebulae and active galactic nuclei* (Sausalito, CA: University Science Books)
- Peimbert, M., Peimbert, A., & Delgado-Inglada, G. 2017, *PASP*, 129, 082001, doi: [10.1088/1538-3873/aa72c3](https://doi.org/10.1088/1538-3873/aa72c3)
- Pradhan, A. K., & Nahar, S. N. 2015, *Atomic Astrophysics and Spectroscopy* (Cambridge University Press: New York)
- Rynkun, P., Gaigalas, G., & Jönsson, P. 2019, *A&A*, 623, A155, doi: [10.1051/0004-6361/201834931](https://doi.org/10.1051/0004-6361/201834931)
- Salim, S., & Narayanan, D. 2020, *ARA&A*, 58, 529, doi: [10.1146/annurev-astro-032620-021933](https://doi.org/10.1146/annurev-astro-032620-021933)
- Savage, B. D., & Mathis, J. S. 1979, *ARA&A*, 17, 73, doi: [10.1146/annurev.aa.17.090179.000445](https://doi.org/10.1146/annurev.aa.17.090179.000445)
- Schlegel, D. J., Finkbeiner, D. P., & Davis, M. 1998, *ApJ*, 500, 525, doi: [10.1086/305772](https://doi.org/10.1086/305772)
- Shaw, R. A., de La Pena, M. D., Katsanis, R. M., & Williams, R. E. 1998, in *Astronomical Society of the Pacific Conference Series*, Vol. 145, *Astronomical Data Analysis Software and Systems VII*, ed. R. Albrecht, R. N. Hook, & H. A. Bushouse, 192
- Shaw, R. A., & Dufour, R. J. 1995, *PASP*, 107, 896, doi: [10.1086/133637](https://doi.org/10.1086/133637)
- Stellato, B., Banjac, G., Goulart, P., Bemporad, A., & Boyd, S. 2020, *Mathematical Programming Computation*, 12, 637, doi: [10.1007/s12532-020-00179-2](https://doi.org/10.1007/s12532-020-00179-2)
- Storey, P. J., & Hummer, D. G. 1995, *MNRAS*, 272, 41, doi: [10.1093/mnras/272.1.41](https://doi.org/10.1093/mnras/272.1.41)
- Tayal, S. S. 2011, *ApJS*, 195, 12, doi: [10.1088/0067-0049/195/2/12](https://doi.org/10.1088/0067-0049/195/2/12)
- Tayal, S. S., & Zatsarinny, O. 2010, *ApJS*, 188, 32, doi: [10.1088/0067-0049/188/1/32](https://doi.org/10.1088/0067-0049/188/1/32)
- Ueta, T., Mito, H., Otsuka, M., et al. 2019, *AJ*, 158, 145, doi: [10.3847/1538-3881/ab328f](https://doi.org/10.3847/1538-3881/ab328f)

- Ueta, T., Ladjal, D., Exter, K. M., et al. 2014, *A&A*, 565, A36, doi: [10.1051/0004-6361/201423395](https://doi.org/10.1051/0004-6361/201423395)
- van Hoof, P. A. M., van de Steene, G. C., Barlow, M. J., et al. 2010, *A&A*, 518, L137, doi: [10.1051/0004-6361/201014590](https://doi.org/10.1051/0004-6361/201014590)
- Walsh, J. R., & Monreal-Ibero, A. 2020, *Galaxies*, 8, 31, doi: [10.3390/galaxies8020031](https://doi.org/10.3390/galaxies8020031)
- Weingartner, J. C., & Draine, B. T. 2001, *ApJ*, 548, 296, doi: [10.1086/318651](https://doi.org/10.1086/318651)
- Whitford, A. E. 1958, *The Astronomical Journal*, 63, 201, doi: [10.1086/107725](https://doi.org/10.1086/107725)
- Wong, M. H. 2010, Amplitude of fringing in WFC3/UVIS narrowband red filters, Space Telescope WFC Instrument Science Report
- Zhang, Y., Liu, X. W., Wesson, R., et al. 2004, *MNRAS*, 351, 935, doi: [10.1111/j.1365-2966.2004.07838.x](https://doi.org/10.1111/j.1365-2966.2004.07838.x)